Astrocyte GluN2C NMDA receptors control basal synaptic strengths of hippocampal CA1 pyramidal neurons in the *stratum radiatum*

Peter H. Chipman[1,5], Alejandra Pazo Fernandez[1,4], Chi Chung Alan Fung[2,4], Angelo Tedoldi[1], Atsushi Kawai[1], Sunita Ghimire Gautam[1,6], Mizuki Kurosawa[1], Manabu Abe[3], Kenji Sakimura[3], Tomoki Fukai[2] and Yukiko Goda[1,*]

[1]RIKEN Center for Brain Science, Wako-shi, Saitama 351-0198, Japan
[2]Neural Coding and Brain Computing Unit, Okinawa Institute of Science and Technology, Onna-son, Kunigami-gun, Okinawa, 904-0495, Japan
[3]Department of Animal Model Development, Brain Research Institute, Niigata University, Niigata, 951-8585, Japan
[4]These authors contributed equally.
[5]Present address: Department of Biochemistry and Biophysics, University of California, San Francisco, San Francisco, CA 94158, USA
[6]Present address: Shikhar Biotech Pvt. Ltd, Lalitpur, Nepal
*Correspondence: yukiko.goda@riken.jp

Summary

Experience-dependent plasticity is a key feature of brain synapses for which neuronal N-Methyl-D-Aspartate receptors (NMDARs) play a major role, from developmental circuit refinement to learning and memory. Astrocytes also express NMDARs although their exact function has remained controversial. Here we identify a circuit function for GluN2C NMDAR, a subtype highly expressed in astrocytes, in layer-specific tuning of synaptic strengths in mouse hippocampal CA1 pyramidal neurons. Interfering with astrocyte NMDAR or GluN2C NMDAR activity reduces the range of presynaptic strength distribution specifically in the *stratum radiatum* inputs without an appreciable change in the mean presynaptic strength. Mathematical modeling shows that narrowing of the width of presynaptic release probability distribution compromises the expression of long-term synaptic plasticity. Our findings suggest a novel feedback signaling system that uses astrocyte GluN2C NMDARs to adjust basal synaptic weight distribution of Schaffer collateral inputs, which in turn impacts computations performed by the CA1 pyramidal neuron.

Key words

Basal synaptic strength; Hippocampus; Astrocytes; NMDA receptors; GluN2C; Layer-specificity; Synaptic plasticity; *Stratum radiatum*

Introduction

Plasticity is a fundamental feature of neuronal connections in the brain, where experience-dependent changes in synaptic strengths over different time scales are crucial for a variety of processes ranging from neural circuit development, circuit computations to learning and memory (Feldman and Brecht, 2005; Bliss and Collingridge, 1993; Abbott and Regehr, 2004; Collingridge et al., 2010; Nicoll, 2017). Deciphering how neurons dynamically express different forms of synaptic plasticity while ensuring the optimal performance of the circuit remains a key challenge (Vitureira and Goda, 2013; Turrigiano, 2017; Nicoll, 2017; Brunel, 2016). In particular, the distribution of synaptic strengths is thought to reflect the capacity or the state of information storage of neural circuits (Barbour et al., 2007; Buzsáki and Mizuseki, 2014; Bromer et al., 2018). A better understanding of the cellular mechanisms that regulate synaptic strength distribution could therefore provide novel insights into the basis for the effective execution of circuit operations (Barbour et al., 2007).

The N-methyl-D-aspartate receptors (NMDARs) are a major ionotropic glutamate receptor type mediating excitatory synaptic transmission (Paoletti et al., 2013; Sanz-Clemente et al., 2013; Hansen et al., 2018). NMDARs are heteromeric assemblies consisting of four subunits, and seven NMDAR subunit genes have been identified that fall into three subfamilies: *Grin1* encoding the obligatory GluN1 subunit, four *Grin2* genes encoding GluN2A-D, and two *Grin3* genes encoding GluN3A-B (Paoletti et al., 2013; Hansen et al., 2018). The differing subunit compositions confer NMDARs with distinct biophysical and pharmacological properties and contribute to their diverse biological activities. NMDARs are expressed throughout the central nervous system (CNS) and are crucial for normal brain function and plasticity. In particular, NMDARs that are typically composed of two GluN1 and two GluN2 subunits and are present postsynaptically have been extensively studied for their role in memory mechanisms (Paoletti et al., 2013; Sanz-Clemente et al., 2013; Nicoll 2017). NMDARs are also involved in pathological conditions such as epilepsy, ischemia, and traumatic brain injury (Hansen et al., 2017). In stark contrast to the multifaceted functions of neuronal NMDARs, very little is known of NMDAR functions in glial cells in the CNS. Amongst the better characterized glial NMDARs, NMDARs in oligodendrocytes play a role in axonal energy metabolism (Saab et al., 2016) and exacerbate pathological conditions (Karadottir et al., 2005). In astrocytes, NMDARs have been long thought to be absent except following ischemia *in vivo* or under anoxia *in vitro* that promote their aberrant expression (Krebs et al., 2003; Gottlieb and Matute, 1997). Nevertheless, there are reports of GluN2C mRNA expression in astrocytes in the adult brain (Watanabe et al., 1993; Karavanova et al., 2007; Ravikrishnan et al., 2018), and several studies provide physiological evidence in support of astrocyte NMDAR expression under non-pathological conditions (Schipke et al., 2001; Serrano et al., 2008; Lalo et al., 2006; Letellier et al., 2016). The precise function for astrocyte NMDARs, however, has

remained a matter of debate (e.g. Kirchhoff, 2017), and the role for astrocyte GluN2C has not yet been identified.

Astrocytes regulate a diverse set of essential brain activities, from neurovascular coupling, metabolic support, and ionic homeostasis (e.g. Attwell et al., 2010; Giaume et al., 2010; Simard and Nedergaard, 2004) to synaptic connectivity and function (e.g. Araque et al., 2014; Clarke and Barres, 2013). Recent studies have highlighted a role for astrocytes in the bidirectional control of basal synaptic transmission (Panatier et al., 2011; Perea and Araque; 2007; DiCastro et al., 2011; Martin-Fernandez et al., 2017; Schwarz et al., 2017), which likely involves signaling via their perisynaptic processes (Bindocci et al., 2017; Bazargani and Attwell, 2016). Moreover, mounting evidence suggests that astrocytes are not only capable of either simply potentiating (Panatier et al., 2011; Perea and Araque, 2007; Jourdain et al., 2007) or depressing synaptic transmission (Martín et al., 2015; Pascual et al., 2005), but a single astrocyte, which contacts tens of thousands of synapses, can concurrently mediate bi-directional synapse regulation at separate synaptic contact sites (Schwarz et al., 2017; Covelo and Araque, 2018). Astrocytes likely regulate neural circuit functions at multiple levels, as suggested by observations of both local and global astrocyte signaling that are triggered in a synapse, neuron, or circuit-specific manner (Martín-Fernandez et al., 2017; Martín et al., 2015; Chai et al., 2017; Deemyad et al., 2018; Dallérac et al., 2018; Santello et al., 2019). However, despite these advances, the basic mechanisms by which astrocytes detect and adjust synaptic transmission and the extent of their impact on local synaptic circuit activity are not fully understood.

Astrocytes express a plethora of neurotransmitter receptors and membrane transporters that are thought to modulate synaptic transmission (Araque et al., 2014; Bazargani and Attwell, 2016), including perisynaptic astrocyte glutamate transporters that influence the magnitude and kinetics of postsynaptic glutamate receptor activation and membrane depolarization (Pannasch et al., 2014; Murphy-Royal et al, 2015) and astrocyte metabotropic glutamate receptors (mGluRs) whose activation promote gliotransmitter release to provide feedback control of synaptic transmission (Panatier et al., 2011; Schwarz et al., 2017; Covelo and Araque, 2018; Araque et al., 2014; Bazargani and Attwell, 2016). Given the often shared expression of neurotransmitter receptors and transporters between astrocytes and neurons, an important challenge is to decipher the synaptic activity-dependent functions of astrocyte receptors and transporters independently of the functions of their neuronal counterparts. Notably, many of the prior studies have focused on pathological brain states (Krebs et al., 2003; Gottlieb and Matute, 1997) or used young brain tissue (e.g. Panatier et al., 2011) or culture preparations (e.g. Schwarz et al., 2017) in which the expression pattern of the astrocyte receptors and channels differ substantially from the adult brain in basal conditions (Sun et al., 2013; also see Boisvert et al., 2018). Consequently, the

92 cellular basis and the network consequences of astrocyte-synapse interactions mediated by the
93 astrocyte receptors and channels in the healthy adult brain remain to be clarified.
94 In a previous study, we identified a role for astrocyte signaling in regulating synaptic
95 strength heterogeneity in hippocampal neurons, which involved astrocyte NMDARs (Letellier et
96 al., 2016). Heterogeneity was assessed by comparing the presynaptic strengths of two
97 independent inputs to pyramidal neurons, which was estimated by the paired-pulse ratio (PPR)
98 of excitatory postsynaptic current (EPSC) amplitudes, a parameter inversely related to
99 presynaptic release probability (Dobrunz and Stevens, 1997). Although basal PPRs were
100 uncorrelated between the two inputs, surprisingly, inhibiting astrocyte NMDARs promoted the
101 correlation of PPRs. This indicated that astrocyte NMDARs contributed to enhancing the
102 differences in basal presynaptic strengths represented by the two different inputs (Letellier et al.,
103 2016). Such pair-wise comparison of PPRs, however, is limited to providing an indirect measure
104 of variability, and it remains unclear how astrocyte NMDARs control the overall shape of the PPR
105 distribution. Furthermore, the crucial roles for neuronal NMDARs in regulating synaptic
106 transmission and plasticity have confounded the interpretation of astrocyte NMDAR functions,
107 which still remain enigmatic (Kirchoff, 2017). Here, we further investigated astrocyte NMDAR-
108 dependent regulation of synaptic strength in hippocampal CA1 pyramidal neurons in adult mice,
109 focusing on the mode of regulation of presynaptic strength distribution, the NMDAR type
110 responsible, and probing the potential layer specific regulation in area CA1. Our findings identify
111 a role for astrocyte GluN2C NMDARs in maintaining broad presynaptic strength diversity
112 specifically in the *stratum radiatum* (SR) by enhancing both strong and weak synapses.
113 Mathematical modeling suggests that presynaptic strength diversity strongly influences the
114 expression of long-term synaptic plasticity, which in turn, is important for network stability and
115 learning and memory (Malenka and Bear, 2004; Collingridge et al., 2010; Royer and Paré, 2003;
116 Zenke and Gerstner, 2017). Our findings suggest astrocyte GluN2C NMDARs as a key player in
117 linking the regulation of synaptic strength distribution to the expression of synaptic plasticity that
118 promotes optimal circuit performance.
119
120 **Results**
121 *NMDAR-dependent regulation of PPR variability in hippocampal CA1 pyramidal neurons*
122 In order to characterize the properties of astrocyte NMDAR-dependent modulation of synaptic
123 strength, here we devised a simplified assay using a single stimulating electrode to monitor PPR
124 variability of Schaffer collateral synapses. Hippocampal slices were prepared from adult mouse
125 brain (P60-120), and EPSCs to a pairwise stimulation (50 ms inter-stimulus interval) of Schaffer
126 collateral axons were recorded in CA1 pyramidal neurons (Figure 1A; Figure S1). MK-801 (1 mM)
127 was infused into the postsynaptic cell via the patch pipette, and after 10-15 min but prior to

128 starting the experiment, Schaffer collaterals were stimulated at 0.1 Hz for at least 45 times to pre-
129 block synaptic NMDARs. This resulted in over 92% inhibition of synaptic NMDAR currents
130 (Bender et al 2006) (Figure S1; see methods). Upon confirming the block of postsynaptic NMDARs,
131 the baseline EPSC recordings were taken; subsequently NMDAR inhibitors were bath applied to
132 test their effects on PPR variance. Under the block of postsynaptic NMDARs, any effects of NMDAR
133 inhibitors, if observed, would be expected to reflect the influence of NMDARs present either in
134 astrocytes or the presynaptic neurons. Notably, in mature brains which we used for our
135 experiments, the contribution of presynaptic NMDARs in general had been suggested be minimal
136 (Shih et al., 2013). Upon bath applying MK801 (50 μM) or AP5 (50 μM), the population variance
137 (δ^2) of PPRs was reduced without a significant change in the mean ($\bar{x}$) (Figure 1B-D; MK801 δ^2
138 p=.016, $\bar{x}$ p=.856; AP5, δ^2 p=.047; $\bar{x}$ p=.162). This overall decrease in PPR variance, when
139 examined at the level of individual inputs, was associated with a change in PPR (ΔPPR) that was
140 negatively correlated to the baseline PPR: PPR of some inputs increased while others decreased
141 by the NMDAR antagonist application (Figure 1E-G). Furthermore, consistent with a lack of change
142 in the mean PPR upon blocking NMDARs, a linear fit to the data intercepted the x-axis near the
143 baseline mean PPR (x-axis intercept: MK801 = 1.97; AP5 = 1.95).
144 We also tested for the contribution of GluN2B NMDAR and also of mGluR5 in maintaining
145 PPR variance. Bath applying Ro25-6981 (10 μM), a GluN2B-specific NMDAR antagonist (Fischer
146 et al., 1997), and MPEP (25 μM), an mGluR5-specific antagonist (Gasparini et al., 1999), had little
147 effect on PPR variance (Figure S2A-C; Ro256981 p=.362, MPEP p=.349). MPEP, however,
148 significantly increased the mean PPR (Figure S2C; p=.033), which is consistent with a reported
149 role for mGluR5 in presynaptic strength regulation (Panatier et al 2011).
150 We next examined whether the changes in PPR elicited by the extracellularly applied
151 NMDAR inhibitors accompanied changes in the EPSC amplitude and the coefficient of variation
152 (CV) of EPSC amplitude, the latter as an additional measure of the change in presynaptic release
153 probability (Malinow and Tsien, 1990; Larkman et al, 1992). On average, bath applied MK801 did
154 not substantially alter the amplitude of the first EPSC to the pair of stimuli relative to control slices,
155 despite a small tendency for an increase with a time delay (Figure 1I; p= .657). MK801 also had
156 little effect on CV^{-2} of EPSC amplitudes (Figure S3B; p= .991), although the responses of individual
157 inputs to MK801, albeit small in magnitude, were positively correlated to CV^{-2} (Figure S3D;
158 Pearson's r = .420, p = .026) and negatively correlated to PPR (Figure S3H; Pearson's r = -.474, p
159 = .011). These data are consistent with the possibility that the observed reduction in PPR diversity
160 by MK801 application is associated with normalization of presynaptic release probability.
161 In contrast to MK801, AP5 significantly increased EPSC amplitudes within 10 min of
162 application (Figure 1J; p = .026), and the increase in CV^{-2} (Figure S3B; AP5 p = .003) suggested that
163 the change in EPSC amplitude involved a presynaptic change. Notably, Ro25-6981 that had no

164 effect on PPR variance, did produce a significant increase in CV^{-2} (Figure S2H; CV^{-2} p = .002), and
165 produced a small but non-significant increase in EPSC amplitudes (Figure S2E; EPSC p = .261),
166 which was consistent with the observed increase in PPR (above). None of the NMDAR antagonists
167 caused substantial changes in the amplitude or frequency of spontaneous EPSCs (sEPSCs) or
168 evoked EPSC waveforms (Figure S4).
169 We next sought to confirm the NMDAR-dependent modulation of presynaptic strength
170 diversity as described in our previous study by comparing PPRs across two independent Schafer
171 collateral inputs that converge onto a target CA1 pyramidal neuron (Letellier et al., 2016), and to
172 observe the time course of PPR population variance change by NMDAR antagonists. In this
173 method, the absolute difference of PPRs between the two inputs (PPR disparity) is taken as a
174 proxy for presynaptic strength variability, with lower PPR disparity indicating lower PPR
175 variability and vice versa (Figure S5A,B). Consistent with our analysis thus far, bath application of
176 MK801 and AP5 reduced PPR disparity (Figure S5D-F; MK801 p = .001, AP5 p=.004), while Ro25-
177 6981 and MPEP did not (Figure S5G,H; Ro25-6981 p = .670, MPEP p = .263).
178 Collectively, these findings support the idea NMDARs play a role in bi-directionally
179 regulating presynaptic strengths to broaden the variability of PPR. Moreover, such an involvement
180 of NMDARs in presynaptic regulation is distinct from the presynaptic regulation by mGluR5 that
181 potentiates synaptic strength across a synapse population.
182
183 *Astrocyte NMDARs mediate the effects of NMDAR antagonists on PPR diversity*
184 To test the extent to which bath applied NMDAR antagonists affected synaptic transmission by
185 targeting astrocyte NMDARs, we knocked down in astrocytes, the *GRIN1* gene that encodes GluN1,
186 a requisite subunit for the cell surface expression of NMDARs (Fukaya et al., 2003; Abe et al.,
187 2004). AAV carrying either mCherry-tagged nlsCre (Cre) or a control nls-mCherry lacking Cre
188 (ΔCre) under the GFAP104 promoter was injected bilaterally into the dorsal hippocampus of adult
189 *GRIN1* floxed mice (Figure 2A)(Letellier et al., 2016). We used low titer AAVs (~0.4-4E10 genome
190 copies/injection) to avoid potential reactive astrocytosis, and although the extent was modest, we
191 obtained a highly specific mCherry expression in astrocytes throughout the area CA1 with little
192 expression in neurons (Figure 2B: Cre, 41.1 ± 2.4% of GFAP+ve cells [n = 3529], 0.3 ± 0.1% of
193 NeuN+ve cells [n = 1150] from 5 mice; ΔCre, 40.7 ± 1.9% of GFAP+ve cells [n = 3309], 0.5 ± 0.1%
194 of NeuN+ve cells [n = 1217] from 5 mice). The efficacy of GluN1 knock-down in astrocytes was
195 assessed electrophysiologically by patch-clamping astrocytes and monitoring slow depolarizing
196 responses elicited by puff applying NMDA and glycine (1mM each) (Figure S6)(Letellier et al.,
197 2016). Astrocytes that expressed Cre as identified by the mCherry fluorescence in *stratum*
198 *radiatum* (SR) where Schafer collateral synapses were present, showed depolarizing responses to
199 NMDA-glycine puff that were significantly decreased compared to ΔCre controls (Figure S6A; p =

200 0.006). Given that mCherry-positive astrocytes were present throughout the CA1, we also
201 monitored NMDA-glycine puff responses in astrocytes in *stratum oriens* (SO) and *stratum*
202 *lacunosum moleculare* (SLM). In contrast to mCherry-positive astrocytes in SR, mCherry-labelled
203 astrocytes in SO or SLM showed depolarizing responses to NMDA-glycine puff that were not
204 different between Cre and control ΔCre slices (Figure S6B-C; SO p = .247; SLM p = .268), despite
205 the fact that viral transduction efficiencies were comparable amongst astrocytes across the three
206 layers (SR: Cre 39.8 ± 2.4%, ΔCre 40.2 ± 2.0%; SO: Cre 44.8 ± 3.0%, ΔCre 39.3 ± 5.9%; SLM: Cre
207 39.1 ± 4.9%, ΔCre 40.0 ± 4.0%). The input resistance of patched astrocytes was not altered by Cre
208 expression in any layer (Figure S6D). Notably NMDA-glycine responses in SLM were substantially
209 smaller than those in SR or SO (p = 0.001, one way ANOVA, Bonferroni post-hoc tests).
210 Nevertheless, AP5 bath application blocked NMDA-glycine puff-induced depolarizing responses
211 in astrocytes in all three layers. This observation suggests that NMDARs are broadly expressed
212 across hippocampal CA1 astrocytes. Moreover, the differential sensitivity of the slow depolarizing
213 responses to astrocyte GluN1 knock-down between layers supports the possibility that the
214 cumulative actions of signaling downstream to NMDAR activation including the contribution of
215 voltage-gated conductances (Serrano et al., 2008; Letellier et al., 2016; Shih et al., 2013) could be
216 heterogeneous across layers. We will return to this layer-specific differences later.
217 Having detected GluN1-dependent functional NMDAR activity in SR CA1 astrocytes, we
218 next asked whether the GluN1 knock-down also affected synaptic transmission of Schaffer
219 collateral synapses similarly to the bath applied NMDAR antagonists. Baseline PPR showed a
220 significantly reduced PPR variance in Cre-infected slices compared to control slices without a
221 change in the mean PPR (Figure 2C,D; δ^2 p = .033; $\bar{x}$ p = .725). Analysis of the relative PPR from
222 two independent Schaffer collateral inputs also revealed lower PPR disparity in Cre injected slices
223 compared to control slices (Figure S7A; p = .009). These observations are consistent with a
224 reduced PPR variance upon compromising astrocyte NMDAR signaling as observed with bath
225 applied NMDAR inhibitors. The amplitude and frequency of spontaneous EPSCs and the waveform
226 of evoked EPSCs were unaltered by astrocyte-specific GluN1 knock-down (Figure S7B,C).
227 We next determined whether astrocyte GluN1 knock-down could occlude the effects of
228 bath applied AP5 on PPR variance, by recording from postsynaptic CA1 neurons infused with
229 MK801 in ΔCre and Cre-infected slices. Similarly to naïve slices, in ΔCre control slices, AP5
230 decreased the population variance of PPRs by strengthening some synapses and weakening
231 others (Figure 2E; ΔCre +AP5 p = .017). In addition, AP5 caused also a variable increase in EPSC
232 amplitudes (Figure 2G; AP5 p = .005) that occurred without a concomitant change in the
233 amplitude or the frequency of spontaneous EPSCs (Figure S7D-G). In Cre slices, however, the
234 decrease in PPR variance by AP5 was strongly attenuated, despite the modest extent of virus
235 infection in Cre slices (Figure 2F; Cre +AP5 p = .789). The analysis of PPR disparity across two

236 inputs also showed substantially decreased inhibitory effect of AP5 in Cre slices relative to
237 controls (Figure S7H-K; ΔCre +AP5 p = .013, Cre +AP5 p =.315). Curiously, the small increase in
238 EPSC amplitudes observed upon applying AP5 was also attenuated in Cre slices (Figure 2H). This
239 suggests that although the effect of NMDAR antagonists on PPR diversity and EPSC amplitudes are
240 likely to target distinct compartments – presynaptic and postsynaptic – both mechanisms may
241 involve astrocyte NMDARs. Together, these observations indicate that astrocyte NMDARs are the
242 major mediators of the synaptic effects of acutely blocking NMDARs in our experimental
243 conditions, and further support the view that astrocyte NMDARs help maintain the broad
244 variability of presynaptic strengths across a synapse population.
245
246 *Modelling of release probability variability reveals its impact on synaptic plasticity*
247 In order to gain an insight into the physiological role for the broad release probability distribution,
248 we sought to assess the impact of reducing the presynaptic strength variability on a synaptic
249 learning rule by constructing a mathematical model. We first modelled release probability
250 variations based on log-normal distributions (Buzsáki and Mizuseki, 2014; Branco and Staras,
251 2009; Murthy et al., 1997) for a range of peak release probability distributions ($U_{\max}$) that
252 represented the control condition and when the variance was reduced to mimic conditions of
253 astrocyte NMDAR blockade, termed "control" and "NMDAR blocked", respectively (Figure 3A; see
254 Methods). The optimal parameters for the log-normal distributions were obtained from the best
255 fit to a modified synaptic facilitation model based on Tsodyks et al. (1998) using the experimental
256 data in which the peak EPSC amplitudes to repetitive stimulation of the Schaffer collaterals at 20
257 Hz were monitored under identical conditions to the PPR experiments (Figure S8A; see Methods).
258 Next, we used the BCM learning rule (Bienenstock et al., 1982) to investigate potential
259 implications of altering the variance of release probability on long-term synaptic plasticity. In the
260 BCM learning rule, the synaptic weight undergoes changes according to the excitatory
261 postsynaptic current and the presynaptic neurotransmitter release, in which the magnitude and
262 the type of long-term plasticity can be controlled by a set of parameters (see Methods). In
263 simulations, we explored the effect caused by decreasing the variance of the release probability
264 on both long-term potentiation (LTP) and long-term depression (LTD). Figure 3B illustrates an
265 example experiment for $U_{\max}$ = 0.1, where traces of the synaptic weight function $w(t)$ for LTP and
266 LTD are two conditions that differ only with respect to the release probability variance of the
267 presynaptic neuron. Application of 100 presynaptic spikes with 50-ms inter-spike intervals
268 triggered a rapid change in synaptic weight during the stimulation that was stably maintained
269 after the stimulation for both LTP and LTD (Figure 3B). Although the efficacy of both LTP and LTD
270 are reduced in the condition of less variable release probability mimicking the NMDAR-block
271 situation, the effect is larger for LTP.

We next sought to test whether the qualitative result of the simulation is preserved over a range of LTP and LTD (i.e. for a series of parameter α; see Methods). To this end, the difference of synaptic weight change induced by stimulation between conditions of broad (control) vs. narrow (NMDAR block) release probability variability was considered as a function of a range of the absolute change in synaptic weight $w(t)$ under control release probability conditions for both LTP and LTD (Figure 3C, solid lines). In the numerical exploration, we found that LTD was always smaller if the pre-synaptic neuron had less variable release probability. In contrast, the sensitivity of LTP to release probability variance depended on the magnitude of potentiation, in which the adverse effect of the narrowing of release probability distribution in compromising synaptic plasticity was increasingly pronounced with a larger degree of potentiation. The robustness of the observed sensitivity of LTP and LTD to the differences in release probability variance was further tested by changing the peak release probability $U_{\max}$ under the same conditions ($U_{\max}$ = 0.10, 0.15, 0.20). The overall pattern of the decrease in the efficacy of LTP and LTD persisted upon narrowing the release probability distribution. However, the reduction of LTD became less prominent when $U_{\max}$ was increased (Figure 3C).

In order to determine whether the influence of release probability variance on the efficacy of long-term plasticity could be observed in a different model, spike-timing dependent plasticity (STDP) was simulated using synaptically connected two leaky integrate-and-fire (LIF) neurons (see Methods). The presynaptic neuron received a spike train of 500 mA magnitude, A_1, while the postsynaptic neuron received a spike train of variable magnitude A_2. Pairing 10 spikes at 20 Hz with a time difference between spike trains of Δt resulted in LTP or LTD, with positive Δt values producing LTP and negative Δt values resulting in LTD (Figure 3D(i)). Notably, conditions that mimic decreased release probability variance seen in NMDAR-blocked experiments showed no observable changes in LTD whereas LTP was compromised compared to control conditions (Figure 3D(ii)), the latter effect on LTP being similar to the observations in the BCM-like model.

Finally, the impact of narrowing the release probability variance was explored under a more general STDP scenario by examining synaptic weight changes elicited in a pair of neurons receiving Poisson spike trains. Specifically, the synaptic weights obtained in response to the same Poisson sequences in the control condition or the NMDAR-blocked condition for a number of independent simulations at $U_{\max}$ of 0.10 showed that the efficacy of potentiation was consistently smaller in the NMDAR-blocked condition (Figure 3E). Such an attenuating effect of the reduced release probability variance on potentiation was observed also when the peak of release probability distributions was shifted to larger values ($U_{\max}$ = 0.15 and 0.20; Figure S8C).

Altogether, the numerical simulation experiments demonstrate that a reduced variability in presynaptic release probability can reshape the long-term synaptic plasticity dynamics. In the BCM-like model, both LTP and LTD were reduced, and in the LIF-neuron-pair model, LTP was

308 reduced whereas LTD appeared largely unchanged. Collectively, LTP is likely to be compromised
309 across a synapse population when the distribution of release probability is narrowed, while the
310 effect on LTD could depend on the fine detail of the spike sequence.
311
312 *Hippocampal astrocytes express GluN2C NMDARs*
313 Our results thus far point to astrocyte NMDARs, and in particular, the involvement of the
314 obligatory subunit GluN1 in regulating the variability of presynaptic strengths. In order to obtain
315 direct molecular evidence for the expression of NMDAR in hippocampal astrocytes and to clarify
316 the relevant NMDAR subtype, we performed single cell RT-PCR to compare the expression of
317 GluN1, GluN2A, GluN2B and GluN2C mRNAs in CA1 astrocytes across SO, SR and SLM layers and
318 CA1 pyramidal neurons (Figure 4A). Acute hippocampal slices were prepared from adult mice as
319 used for electrophysiology experiments, and after labelling astrocytes with sulforhodamine101
320 (Nimmerjahn et al., 2004), RNA from single cells was extracted by patch-clamping. All putative
321 astrocytes had low input resistances (SR 11.20 ± 0.36 MΩ; SO 13.24 ± 0.43 MΩ; SLM 10.60 ± 0.33
322 MΩ; n = 39 cells, 9 mice sampled for each layer), lacked action potentials, and displayed linear
323 current-voltage relationships (Figure 4A,B). CA1 pyramidal neurons expressed high levels of
324 GluN1, GluN2A and GluN2B subunit mRNAs but expressed substantially low levels of GluN2C
325 mRNA. In contrast, astrocytes in all three layers showed robust expression of GluN2C mRNA.
326 Moreover, astrocytes showed minimal expression of GluN2A and GluN2B mRNAs, and the GluN1
327 mRNA expression in astrocytes was also substantially low compared to neurons (Figure 4C).
328 GluN2D mRNA in CA1 pyramidal neurons and astrocytes was also tested, and it was undetectable
329 in RNA extracted from patch clamping both cell types while the probe itself could detect GluN2D
330 mRNA in brain tissue extracts (data not shown). Inability to detect GluN2D mRNA in astrocytes is
331 consistent with previous reports of single cell RNA-seq analysis (Khakh Lab database; also see
332 Alsaad et al., 2019). We also examined the levels of expression of NMDAR subunits in CA3
333 pyramidal neurons, and the pattern of subunit expression mirrored the pattern observed for CA1
334 pyramidal neurons with little expression of GluN2C and GluN2D mRNAs, but higher levels of
335 GluN1, GluN2 and GluN2B mRNAs (data not shown).
336 The expression of GluN2C subunit protein in the hippocampus was confirmed by
337 immunoprecipitation of mouse hippocampal extracts followed by Western blotting, using Cre that
338 is not expressed in wild type mice as a negative control (Figure 4D). For characterizing the cellular
339 expression pattern of GluN2C in the hippocampus, we were unable to identify an antibody against
340 GluN2C that was suitable for immunofluorescence labelling experiments. Therefore, in order to
341 visualize the cells that expressed GluN2C, we used a GluN2C mutant mouse line carrying an
342 insertion of a codon-improved Cre recombinase immediately downstream of the translation
343 initiation site in the *GRIN2C* gene (Miyazaki et al., 2012). GluN2C-Cre mice were crossed with a

344 Cre reporter line (Ai9: Madisen et al., 2010) that expressed tdTomato upon Cre-mediated
345 recombination. The hippocampus of the offspring showed robust tdTomato fluorescence in
346 astrocytes identified by GFAP labelling (81.6 ± 5.7% of GFAP+ve cells; Figure 4E,F), which was
347 consistent with the high expression level of GluN2C mRNA in astrocytes (Figure 4C). Moreover,
348 some interneurons in SR identified by the NeuN labeling also expressed tdTomato (3.6 ± 1.6% of
349 NeuN+ve cells in SR, Figure 4E,F), which was in agreement with previous reports (Ravikrishnan
350 et al., 2018; Gupta et al., 2016). Surprisingly, the pyramidal cell layer also showed sporadic
351 tdTomato-labelled neuronal cell bodies, although such cells represented a limited proportion of
352 pyramidal neurons (5.8 ± 1.0% of NeuN+ve cells in *stratum pyramidale*, Figure 4E,F). The RT-PCR,
353 biochemical and immunohistochemistry experiments collectively provide evidence in support of
354 GluN2C-containing NMDAR as a major NMDAR type expressed in hippocampal CA1 astrocytes.
355
356 *Inhibition of GluN2C NMDARs reduces PPR variability in a manner sensitive to astrocyte GluN1*
357 *expression*
358 Given the prominent expression of GluN2C in astrocytes, we wondered if the regulation of PPR
359 could be attributed to GluN2C NMDARs. To test such a possibility, we examined whether
360 pharmacological inhibition of GluN2C NMDARs could mimic the effects of bath applied AP5 and
361 MK801 on PPR variance using QNZ46 (25 μM), an NMDAR antagonist specific for GluN2C/D
362 (Hansen and Traynelis, 2011). Similarly to MK801 and APV, QNZ46 reduced the population
363 variance of PPRs without altering the mean PPR (Figure 5A; δ^2 p=.008; $\bar{x}$ p=.312). Again we
364 observed the negative correlation between the change in PPR and the baseline PPR (Figure 5B),
365 with a linear fit to the data intercepting the x-axis near the baseline mean PPR (X intercept = 2.07).
366 Additionally, in experiments monitoring two independent Schaffer collateral inputs, bath
367 application of QNZ46 decreased the PPR disparity as found for AP5 and MK801 (Figure S5D-F; p
368 = .005). These observations suggest that GluN2C/D-containing NMDARs contribute to
369 maintaining the broad PPR diversity by weakening stronger inputs and strengthening weaker
370 inputs. Given the lack of detectable expression of GluN2D in hippocampal CA1 cells, it is likely that
371 NMDARs containing GluN2C mediate the observed effects of QNZ46 in bi-directionally modulating
372 presynaptic strength to decrease the variability of PPR.
373 When EPSC amplitudes were examined, QNZ46 bath application caused a significant
374 increase, reminiscent of the changes observed upon AP5 and MK801 application (Figure 5C; p =
375 .014). Moreover, similarly to AP5, QNZ46 significantly increased CV^{-2} of EPSC amplitudes (Figure
376 S4B; p = .009), which was suggestive of presynaptic alterations.
377 Next we asked whether QNZ46 acted on astrocyte NMDARs to control PPR variability. To
378 address this point, we again tested for occlusion using astrocyte GluN1 knock-down slices. QNZ46
379 was bath applied to Cre and ΔCre-infected slices while recording EPSCs from CA1 neurons infused

380 with MK801. In ΔCre control slices QNZ46 decreased the PPR variance (Figure 5D; p = .065) and
381 caused a variable increase in EPSC amplitudes (Figure 5F; QNZ46 p = .005) without a concomitant
382 change in the amplitude or the frequency of spontaneous EPSCs (Figure S7D-G). Crucially, as
383 observed for AP5, QNZ46 was no longer effective in producing a significant change in the PPR
384 variance in Cre slices (Figure 5E; p = .649). When PPR disparity across two inputs was monitored,
385 QNZ46 decreased the PPR disparity in a manner that was sensitive to astrocyte GluN1 knock-
386 down, which also supported the involvement for GluN2C-NMDARs in regulating presynaptic
387 strength diversity (Figure S7H-K; ΔCre +QNZ46 p = .031; Cre +QNZ46 p = .126). Moreover,
388 similarly to AP5, QNZ46-dependent increase of EPSC amplitudes was attenuated also in Cre slices
389 (Figure 5G).
390 Together, these observations indicate that GluN2C NMDARs expressed in astrocytes
391 function to maintain the broad variability of presynaptic strengths across a synapse population.
392 While GluN2C NMDARs also play a role in regulating EPSC amplitudes, this is likely to involve a
393 mechanism that is distinct from the presynaptic regulation but is engaged in parallel to target
394 postsynaptic processes.
395
396 *Layer-specific regulation of synaptic strength by astrocyte NMDARs*
397 Astrocytes are a highly heterogeneous cell type (Zhang and Barres, 2010; Khakh and Sofroniew,
398 2015) that influence synaptic transmission in a synapse- and circuit-specific manner (Martin-
399 Fernandez et al., 2017; Schwarz et al., 2017; Martin et al., 2015; Lanjakornsiripan et al., 2018). Our
400 RT-PCR analysis of NMDAR subtype expression showed relatively high expression of GluN2C
401 mRNA across SR, SO and SLM layers in CA1 astrocytes compared to CA1 pyramidal neurons.
402 Nevertheless, despite the relatively even expression of GluN2C across layers, our NMDA-glycine
403 puff application experiments CA1 astrocytes revealed layer-specific differences in the GluN1-
404 dependent component of the slow depolarizing responses triggered by the NMDA-glycine puff,
405 with SR astrocytes showing the highest sensitivity to the astrocyte GluN1 knock-down (Figure S6).
406 This raised the possibility that astrocyte NMDAR-dependent modulation of synaptic inputs to CA1
407 pyramidal neurons whose dendrites span across SR, SO and SLM, might also differ across layers.
408 To test such possibility of layer-specific regulation, we compared astrocyte NMDAR-
409 dependence of synaptic transmission in CA1 neurons across three layers in slices from astrocyte
410 GluN1 knock-down and control mice. In contrast to the specific decrease in the PPR variance
411 observed in Cre slices relative to ΔCre control slices for the SR input (Figure 2D), neither the PPR
412 variance nor its mean differed between Cre and ΔCre control slices for the SO and the SLM inputs
413 (Figure 6A-D; SO δ^2 p = .303; $\bar{x}$ p = .402; SLM δ^2 p = .624; $\bar{x}$ p = .161). We also examined the layer-
414 specificity of PPR diversity regulation using a pharmacological approach in slices from wildtype
415 mice. The sensitivity of PPRs to bath applied NMDAR antagonists in CA1 pyramidal neurons

intracellularly perfused with MK801, was monitored in response to pairwise stimulation of SO and SLM inputs as had been done for the SR input. Neither MK801 nor AP5 had any appreciable effect on PPR variance in SO and SLM (Figure 6E,G,I,K; SO MK801 p = .107, AP5 p = .472; SLM MK801 p = .920, AP5 p = .741). MK801 modestly increased EPSC amplitudes at some inputs in SO (Figure 6F; p = .783) but it had no effect in SLM (Figure 6J; p = .915). Moreover, AP5 did not potentiate EPSC amplitudes as observed for the SR input, but instead it significantly depressed EPSC amplitudes in SO (Figure 4G; p = .028) while it caused no appreciable change in SLM (Figure 6L; p = .317). Collectively, these results suggest that regulation of PPR diversity by astrocyte NMDARs in CA1 pyramidal neurons is specific to the SR inputs.

As a further test of the layer specificity of astrocyte NMDAR-dependent regulation of PPR variability, we assessed PPR disparity by performing two independent pathway analysis in each layer in response to bath applied NMDAR antagonists. Again, in contrast to SR input (Figure S5D, E), neither MK801 nor AP5 depressed the PPR disparity of the SO and the SLM inputs (Figure S9). These observations are consistent with the role for astrocyte NMDAR - particularly GluN2C NMDARs - for maintaining the diversity of PPR, specifically of SR inputs to CA1 pyramidal neurons.

Discussion

Broad heterogeneity in the efficacy of synaptic transmission is a fundamental feature of small glutamatergic synapses in the mammalian brain (Dobrunz and Stevens, 1997; Atwood and Karunanithi, 2002; Branco and Staras, 2009). A variety of presynaptic parameters contribute to the observed variability, such as the abundance, subtype, and location of presynaptic calcium channels (Thalhammer et al., 2017; Brenowitz and Regehr, 2007; Eltes et al., 2017), their positioning with respect to the synaptic vesicles, the active zone size and the number of docked vesicles, the state of vesicle fusion machinery (Park and Tsien, 2012; Marra et al., 2012; Fulterer et al., 2018; Glebov et al., 2017; Holderith et al., 2012), as well as the coupling to neuromodulatory signals (Burke et al., 2018), and the synapse's recent history of synaptic plasticity. These determinants of presynaptic release efficacy are influenced by target-specific signals (Éltes et al., 2017; Branco et al., 2008; Reyes et al., 1998; Markram et al., 1998) and are further subject to activity-dependent modulation (Thalhammer et al., 2017; Goda and Stevens, 1998; Burke et al., 2018). Although the basis for presynaptic release probability regulation at individual synapses have been intensively studied, whether and how basal release probability variability is collectively controlled across a synapse population is poorly understood, despite its implications in information processing and memory storage (Barbour et al., 2007; Buzsáki and Mizuseki, 2014; Bromer et al., 2018; Rotman and Klyachko, 2013). Our study highlights the novel contribution of astrocyte GluN2C NMDAR signaling in broadening the basal release efficacy of Schaffer collateral

451 synapses by effectively maintaining strong synapses stronger and weaker synapses weaker
452 without an overt effect on the mean synaptic strength.
453 The present study took advantage of paired-pulse response, a short-term plasticity
454 inversely related to presynaptic release probability as a measure of presynaptic efficacy (Dobrunz
455 and Stevens, 1997), which in some experiments was further corroborated by the correlated
456 changes in CV^{-2} (Malinow and Tsien, 1990; Larkman et al., 1992). This study extends the concept
457 of NMDAR-mediated glial control of PPR (Letellier et al 2016) to include populations of synapses
458 within defined hippocampal subregions in the healthy adult mouse brain. Sampling a small
459 number of synapses by a relatively weak stimulation intensity (i.e. mean EPSC amplitude of ~60
460 ± 6 pA to Schaffer collateral stimulation in control condition) consistently revealed a component
461 of PPR distribution that was bi-directionally regulated by astrocyte NMDARs. Notably, such
462 modulation could be masked when sampling a large synapse population that yields stable
463 ensemble responses (Lines et al., 2017). Altogether, results from (i) pharmacological experiments
464 using subtype-specific NMDAR antagonists, which allowed monitoring the effects of NMDAR
465 inhibition in the same synapse population, (ii) the genetic interference specifically of astrocyte
466 NMDARs, and (iii) the cellular expression analysis of NMDAR subunits, collectively point to
467 GluN2C NMDAR as the major astrocyte receptor that regulates synaptic strength variability of
468 Schaffer collateral inputs.
469
470 *Functional significance of the broad distribution of presynaptic strengths*
471 What might be an advantage in maintaining a highly variable presynaptic efficacy across a synapse
472 population of a given input type? Our mathematical modeling and simulation data indicate that
473 the width of release probability distribution can bias the outcome of activity-dependent synaptic
474 plasticity. In the BCM-like model, a broad release probability distribution favors activity-
475 dependent synaptic depression, while for cases involving a large extent increase in synaptic
476 strength, increased release probability variance promotes potentiation. In a spiking neuron
477 model, the increased release probability variance also promoted LTP while the impact on LTD
478 may depend on the fine structure of the spikes. Notably, several studies have implicated astrocyte
479 signaling in LTD in hippocampal CA3 to CA1 synapses (Chen et al., 2013; Andrade-Talavera et al.,
480 2016; Navarrate et al., 2019; Pinto-Duarte et al., 2019), where spike timing-dependent LTD in
481 slices from young mice is sensitive to inhibitors of GluN2C/D, although the source of GluN2C/D
482 remains to be determined (Andrade-Talavera et al., 2016). Astrocyte GluN2C NMDAR-dependent
483 maintenance of variable basal presynaptic strengths of CA3 to CA1 synapses that we have
484 identified here could therefore be linked to astrocyte signaling that promotes LTP and LTD, which
485 in turn, are not only important for learning and memory but also for network stability
486 (Collingridge et al., 2010; Royer and Paré, 2003; Zenke and Gerstner, 2017). Curiously, this

487 GluN2C NMDAR-dependent broadening of the basal presynaptic efficacy in CA1 neurons is
488 confined to the SR inputs and not observed for SO or SLM inputs. This suggests that for dendritic
489 computations in CA1 pyramidal neurons, the broad variability of synaptic strengths at CA3-CA1
490 synapses is more crucial compared to the synaptic strength variability of basal or apical tuft
491 inputs. Mice deficient in GluN2C, while mostly normal in their behavior, show deficits in
492 acquisition of conditioned fear and working memory and changes in neuronal oscillations
493 (Hillman et al., 2011; Mao et al., 2020). Some population of interneurons express GluN2C, however
494 (Gupta et al., 2016; Ravikrishnan et al., 2018), and this confounds the interpretation of the
495 observed effects solely to deficits in astrocyte GluN2C. It would be of interest to determine in the
496 future of whether there is a learning performance deficit in mice specifically deficient in astrocyte
497 GluN2C or GluN1 in the hippocampal CA1 subfield.
498 The mechanism by which astrocyte GluN2C NMDARs are coupled to the changes in
499 presynaptic efficacy remains to be clarified. The bi-directional changes in PPR suggest, in one
500 possibility, that astrocyte NMDAR signaling could trigger the release of two types of
501 gliotransmitters with one potentiating and another depressing (Schwarz et al., 2017; Covelo and
502 Araque, 2018). Interestingly, astrocyte-mediated release of ATP, which is converted to adenosine
503 by extracellular ATPases, has been implicated in the bi-directional modulation of presynaptic
504 efficacy (Panatier et al., 2011; Pascual et al., 2005; Zhang et al., 2003; Tan et al., 2017). The effects
505 of adenosine depend in part on the presynaptic A_{2A} or A_1 receptors that either enhance or
506 suppress presynaptic function, respectively (Panatier et al., 2011; Tan et al., 2017). Similarly, the
507 relative abundance of A_{2A} or A_1 receptors at individual presynaptic boutons could determine the
508 polarity of presynaptic efficacy upon accumulation of extracellular adenosine by the astrocyte
509 GluN2C NMDAR activity. In another scenario, astrocyte GluN2C receptors may influence the
510 release of other gliotransmitters such as glutamate (Jourdain et al., 2007) to target presynaptic or
511 postsynaptic glutamate receptors and/or GluN2C receptor signaling may influence astrocyte-
512 mediated K^+ clearance to locally shape presynaptic action potential waveforms (Cui et al., 2018)
513 to in turn affect presynaptic efficacy.
514
515 *Astrocyte NMDAR subunit mRNAs and implications for layer-specific synapse modulation*
516 Previous transcriptome analysis of the major cell types in mouse cerebral cortex have suggested
517 that the GluN2C NMDAR subunit mRNA is one of the highly enriched transcripts in astrocytes,
518 whose level can be up to 70 fold of the level found in neurons (Zhang et al., 2014). Our single cell
519 RT-PCR analyses also show robust expression of GluN2C mRNA in astrocytes across the three CA1
520 layers in contrast to GluN2C mRNA expression in pyramidal neurons. Curiously, despite the high
521 expression of GluN2C mRNA in astrocytes, only low levels of GluN1 mRNA is detected in
522 astrocytes. This finding is unexpected given that GluN1 subunit is required for the surface

523 expression of functional NMDARs (Fukaya et al., 2003; Abe et al., 2004). Moreover, the observed
524 occlusion of QNZ46 effects on synaptic transmission by astrocyte-specific knock-down of GluN1
525 also support the presence of functional heteromeric GluN1/GluN2C NMDARs in astrocytes. The
526 whole-cell patch clamp method we used to collect RNAs is biased towards sampling of transcripts
527 that are abundant in the cell body. Given that astrocyte processes are numerous and thin, the
528 discordance between the detected GluN1 and GluN2C mRNA levels could be explained if the
529 mRNAs are differentially localized, with GluN1 mRNA being preferentially targeted to processes
530 compared to the cell body of astrocytes. Such a proposal is consistent with a recent study
531 reporting of GluN1 mRNA in astrocyte processes that is locally translated (Sakers et al., 2017). The
532 precise intracellular localization of NMDAR subunit mRNAs in astrocytes remains to be
533 determined.

534 The present study revealed synapse regulation by the astrocyte GluN2C NMDARs that is
535 confined to the SR input although GluN2C mRNA is expressed broadly across CA1 astrocyte layers.
536 Therefore, the layer-specificity of synaptic modulation could potentially arise from features of
537 GluN2C NMDAR assembly and trafficking and/or signaling that is unique to SR astrocytes over SO
538 and SLM astrocytes. In support of layer-specific differences in astrocyte NMDAR signaling, the
539 slow astrocyte membrane depolarization triggered by puff applied NMDA-glycine shows
540 significant dependence on astrocyte NMDAR only in SR and not in SO nor in SLM (Figure S6).
541 Additionally, differences in the properties of presynaptic inputs to CA1 pyramidal neuron
542 dendrites across layers (e.g. Schroeder et al., 2018) could also contribute to layer-specific synaptic
543 modulation by astrocyte GluN2C NMDARs.

544 The GluN2C subunit forms diheteromeric receptor complexes with the obligate GluN1
545 subunit and triheteromeric receptor complexes with GluN1 and GluN2A (Paoletti et al., 2013;
546 Hansen et al., 2018). The presence of GluN2C confers NMDAR properties that are distinct from
547 NMDARs containing GluN2A or GluN2B which are abundant in neurons. For example, GluN2C-
548 containing NMDARs show reduced channel open probability, increased glutamate sensitivity,
549 slow receptor deactivation, and a decreased sensitivity to Mg^{2+} block (Paoletti et al., 2013; Hansen
550 et al., 2018). Weak Mg^{2+} binding would enable open-pore blockers such as MK801, to nonetheless
551 rapidly exert their inhibitory action. Such reduced Mg^{2+} sensitivity of astrocyte NR2C NMDARs
552 could have contributed to the rapid effect observed for MK801 in normalizing presynaptic
553 strengths and reducing the PPR disparity. Moreover, the low EC_{50} of GluN2C-containing NMDAR
554 activation to glutamate (Hansen et al., 2018) suggests that they may be well suited for detecting
555 synaptic release events at perisynaptic astrocyte processes that can be at some distance from the
556 active zone. Several drugs that target NMDARs have been in clinical use, such as ketamine as an
557 anesthetic and treatment for depression (Krystal et al., 2019; Williams and Schatzberg, 2016) and
558 memantine for the treatment of moderate to severe dementia in Alzheimer's disease (Graham et

559 al., 2017). Under physiological conditions, GluN2C/GluN2D-containing NMDARs display up to 10-
560 fold higher sensitivity to ketamine and memantine in comparison to GluN2A/GluN2B-containing
561 NMDARs that are highly expressed in neurons (Kotermanski and Johnson, 2009; Hansen et al.,
562 2017). Therefore, although therapeutics targeting NMDARs to date have largely focused on
563 neuronal NMDARs, it would be crucial to consider also the consequences of interfering with
564 GluN2C NMDARs that are enriched in astrocytes, which is underscored by the increasing
565 recognition of the involvement of astrocytes in a variety of neurological disorders (Zuchero and
566 Barres, 2015; Chung et al., 2015).
567
568
569 **Materials and Methods**
570 *Slice preparation and whole cell recordings*
571 Mice (P60-120) were deeply anesthetized with isoflurane and transcardially perfused with ice-
572 cold cutting aCSF containing (in mM) 93 N-methyl D-glucamine, 2.5 KCl, 1.2 NaH_2PO_4, 30 $NaHCO_3$,
573 20 HEPES, 20 glucose, 5 Na ascorbate, 2 thiourea, 3 sodium pyruvate, 12 N-acetyl L-cysteine, 10
574 $MgSO_4$, 0.5 $CaCl_2$, pH adjusted to 7.4 with HCl and bubbled with 95% O_2 / 5% CO_2. Brains were
575 extracted and 350 µm transverse hippocampal slices were cut in ice-cold cutting aCSF on a Leica
576 VT1200 vibrating microtome. Slices were incubated for 12 min in cutting aCSF warmed to 34°C,
577 then placed in holding solution containing (in mM) 81.2 NaCl, 2.5 KCl, 1.2 NaH_2PO_4, 30 $NaHCO_3$,
578 20 HEPES, 20 D-glucose, 5 Na ascorbate, 2 thiourea, 3 sodium pyruvate, 12 N-acetyl L-cysteine, 2
579 $MgSO_4$, 2 $CaCl_2$, pH 7.4, bubbled with 95% O_2 / 5% CO_2 for up to 8 h. In some cases, slices were
580 incubated in 50 µM sulphorhodamine for 30 min at 34°C to identify astrocytes for RNA extraction.
581 Whole-cell patch clamp recordings were obtained from CA1 pyramidal neurons or
582 astrocytes using an Olympus BX51W1 microscope equipped with IR-DIC optics and a motorized
583 stage. Images were captured with a digital camera (Andor, iXion3) and imaged using MetaMorph
584 software (Molecular Devices). Voltage clamp and current clamp experiments were carried out
585 using Multiclamp 700B amplifiers (Molecular Devices) and up to four micromanipulators (SM5,
586 Luigs and Neumann). Patch pipettes (tip resistance 2-4 MΩ for neurons, 4-6 MΩ for astrocytes)
587 were pulled using a vertical 2-stage puller (PC-10 Narishige). Slices were constantly perfused with
588 recording aCSF containing (in mM) 119 NaCl, 2.5 KCl, 1.3 NaH_2PO_4, 26 $NaHCO_3$, 1 $MgCl_2$, 2 $CaCl_2$,
589 20 D-glucose and 0.5 Na ascorbate pH 7.4, bubbled with 95% O_2 / 5% CO_2 and maintained at 32-
590 34°C using an in-line heater (Harvard Instruments). Picrotoxin (100 µM) was added to the
591 recording aCSF to block $GABA_A$-receptors and isolate glutamatergic synaptic transmission.
592 Internal pipette solution contained (in mM) 130 $CsMeSO_3$, 8 NaCl, 4 Mg-ATP, 0.3 Na-GTP, 0.5
593 EGTA, 10 HEPES, pH 7.3, 290-295 mOsm for neuron recordings, and 130 K gluconate, 10 HEPES,
594 4 $MgCl_2$, 4 Na_2-ATP, 0.4 Na_3-GTP, 10 Na-phosphocreatine, pH 7.3, 290 mOsm for astrocyte

595 recordings. 50 μM AlexaFluor 488 or 594 hydrazide (Thermo Fisher Scientific) was included in
596 the pipette solution to verify cell identity and to position stimulating and puff pipettes. Neurons
597 were voltage clamped at -70 mV and series resistance (R_s) was monitored throughout all
598 recordings and left uncompensated. Experiments were discarded if R_s <30 MΩ and/or changed by
599 >20%. Average R_s was 25.24 ± 0.27 MΩ (n=298 cells).
600
601 *Recordings of synaptic transmission*
602 For all experiments using NMDAR antagonists, 1 mM MK801 was included in the patch pipette
603 solution. Internal solution was allowed to equilibrate into the cell for 10-15 min and inputs were
604 stimulated at a low frequency (0.1Hz) with pairs of pulses at least 45 times before beginning the
605 experiment to pre-block postsynaptic NMDAR receptors. Effective inhibition of NMDAR currents
606 by internal MK801 was confirmed in a separate set of experiments (Figure S1). Pipettes were tip
607 filled with ~0.2 μl of internal solution lacking MK801 to avoid its leakage to the extracellular
608 milieu prior to seal formation. Small bundles of axons in the *stratum radiatum*, *oriens*, or
609 *lacunosum moleulare* were stimulated using AgCl bipolar electrodes in theta-glass pipettes (tip
610 diameter ~2-3 μm) filled with recording aCSF, connected to a stimulus isolation unit (A360, WPI).
611 These bundles are identified throughout as 'input'. Stimulation strengths varied between ~50-
612 500 μA and were adjusted to obtain EPSCs of approximately 50-100 pA. Up to three independent
613 inputs were sampled during a single experiment, though a maximum of two independent inputs
614 were activated per input pathway. When multiple stimulation electrodes were used they were
615 positioned on opposite sides of the neuron and/or in different input pathways (i.e. SR and SLM, or
616 SR and SO). When sampling two inputs in a single pathway, the independence of the two inputs
617 was confirmed by a cross-paired-pulse stimulation paradigm (Letellier et al., 2016); after
618 stimulating one of the two inputs the other input was stimulated in quick succession (50 ms inter-
619 pulse interval). If facilitation or depression was observed in the second pulse, then the position of
620 stimulation electrode was changed and independence of the two inputs was re-assessed. During
621 the experiment, EPSCs from each pathway were sampled with paired pulses every 30 s. Inputs
622 from separate pathways were stimulated at least 5 s apart. EPSCs were sampled over a 10 min
623 baseline period (i.e. 20 sweeps) before the perfusion of drugs and continued for at least an
624 additional 20 min. EPSC amplitudes were averaged over 20 pre-drug baseline sweeps, and 20
625 post-drug sweeps. The change in EPSCs (ΔEPSCs) was calculated as the ratio of the average post-
626 drug amplitude to the average baseline amplitude. PPRs were calculated based on the average
627 EPSCs of 5 sweep bins (i.e. 2.5 min). Baseline and post-drug averages were calculated as the
628 average of four bins (i.e. over 10 min) before and after drug application, respectively. Changes in
629 PPR (ΔPPR) were calculated as the difference between the drug application value and the baseline
630 value. Values for coefficient of variation (CV) were obtained from 20 baseline, and 20 post-drug

631 sweeps. The change in CV^{-2} (ΔCV^{-2}) was calculated as the ratio of post-drug CV^{-2} to pre-drug CV^{-2}.
632 EPSCs and sEPSCs amplitudes in the absence of drug application were stable over the duration of
633 the experiment, and sEPSC amplitudes were stable across all drug conditions tested (Figure S3,
634 S6), suggesting that run-down (i.e. non-stationarities) will not substantially influence the outcome
635 of the CV^{-2} analysis. All EPSC amplitude, rise-time, and decay measurements were performed in
636 Clampfit 10.6 software. sEPSCs were identified as events outside a 50ms window following the
637 second stimulation pulse for each pathway using the template matching algorithm in Clampfit
638 10.6.
639
640 *Astrocyte recordings and NMDA/glycine puff*
641 Astrocytes were identified in acute slices based on mCherry or sulphorhodamine fluorescence, or
642 on their appearance under IR-DIC observation (small, circular cell bodies in the neuropil).
643 Astrocyte identity was always confirmed by their passive electrical properties (linear I-V
644 relationship), low input resistance (<20 MΩ), and low resting membrane potential (< -75 mV), as
645 well as post-hoc labeling by Alexa dyes included in the patch pipette. Recording aCSF contained
646 picrotoxin (100 μM), tetrodotoxin (0.5 μM), and CNQX (10 μM) to reduce network excitability
647 associated with the application of iGluR agonists. Patch pipettes (R_t = 4-6 MΩ) were used to locally
648 deliver recording aCSF solution containing 1 mM NMDA and 1 mM glycine. Puff pipettes were
649 placed approximately 50 μm from the patched cell and puff pressure (3 psi, 100 ms duration) was
650 controlled with a Picospritzer III (Parker Hannifin) connected to N_2 gas.
651
652 *Whole-cell patch RNA extraction from astrocytes and neurons*
653 Whole-cell patch clamp recordings from astrocytes and neurons were performed using pipettes
654 containing (in mM) 130 K gluconate, 10 HEPES, 4 $MgCl_2$, 4 Na_2-ATP, 0.4 Na_3-GTP, 10 Na-
655 phosphocreatine, 1U/μL RNAase inhibitor, 50 μM AlexaFluor488, pH 7.3, 290 mOsm. Pipettes
656 were tip filled (~0.2 μl) with the same internal solution but lacking RNAase inhibitor in order to
657 facilitate obtaining of GΩ seals. After determining the electrical properties of the patched cell to
658 confirm its identity, RNA was extracted using a previously published protocol (Fuzik et al., 2015).
659 The cell was held at -5 mV, and repetitively depolarized to +20 mV for 5 ms at 100 Hz for ~5 min
660 while light negative pressure was applied to the pipette. The AlexaFluor fluorescence signal was
661 visualized to confirm the extraction of cell cytoplasm.
662
663 *Single cell quantitative PCR*
664 Individual patched cells were processed following the provider´s recommendation for the Single
665 Cell-to-CT™ qRT-PCR Kit (ThermoFisher Scientific). cDNAs for GRIN1, GRIN2A, GRIN2B, GRIN2C,
666 GRIN2D and Rn28s1 were quantified by TAQMAN system using the following probes. The

667 provider's recommended pre-amplification step was performed for all the genes except for
668 Rn28s1.
669
670 GRIN1 fw 5'GACCGCTTCAGTCCCTTTGG 3', rv 5' CACCTTCCCCAATGCCAGAG 3', probe 5'
671 AGCAGGACGCCCCAGGAAAACCAC 3' (MGBNFQ, 6FAM)
672
673 GRIN2A fw 5' AGACCCCGCTACACACTCTG 3', rv 5'TTGCCCACCTTTTCCCATTCC 3', probe
674 5'AGCACGATCACCACAAGCCTGGGG 3' (MGBNFQ, 6FAM)
675
676 GRIN2B fw 5'GGCATGATTGGTGAGGTGGTC 3', rv 5'GGCTCTAAGAAGGCAGAAGGTG 3', probe
677 5'ATTGCTGCGTGATACCATGACACTGATGCC 3' (MGBNFQ, 6FAM)
678
679 GRIN2C fw 5'GGAGGCTTTCTACAGGCATCTG 3', rv 5'ATACTTCATGTACAGGACCCCATG 3',
680 probe 5'TCCCACCGTCCCACCATCTCCCAG 3' (MGBNFQ, 6FAM)
681
682 GRIN2D fw 5'TCAGCGACCGGAAGTTCCAG 3', rv 5'TCCCTGCCTTGAGCTGAGTG 3', probe
683 5' TCCTCCACTCTTGGCTGGTTGTATCGCA 3'(MGBNFQ, 6FAM)
684
685 Rn28s1 fw 5'CCTACCTACTATCCAGCGAAACC 3', rev 5'AGCTCAACAGGGTCTTCTTTCC 3', probe 5'
686 CTGATTCCGCCAAGCCCGTTCCCT 3' (MGBNFQ, VIC)
687
688 RNA levels were normalized by the quantity of Rn28s1, and standard curves were prepared for
689 estimating the quantity (in femtograms) of the targeted RNAs after pre-amplification. For making
690 the standard curves, total RNA from mouse brain hippocampal tissue was extracted using TRIZOL
691 reagent. Target cDNAs were amplified by regular PCR, and amplicons were purified, quantity of
692 cDNA was measured and submitted to serial dilutions, used for standard curves in TAQMAN
693 system, in parallel to the single cell derived cDNA samples.
694
695 *Intracranial AAV injections*
696 Recombinant AAV vectors were targeted to the dorsal CA1 hippocampus of adult (P60-P90)
697 GRIN1$^{flx/flx}$ mice as previously described (Letellier et al., 2016; Cetin et al., 2007). Bilateral
698 injections (~600 nl/hemisphere at a rate of 200 nl/min) of AAV9.2-GFAP104-nls-mCherry-Cre
699 (6.67×10^{13} genome copies/ml), AAV9.2-GFAP104-nls-mCherry (i.e. ΔCre; 6.86×10^{13} genome
700 copies/ml), AAVDJ8-GFAP104-nls-mCherry-Cre (5.95×10^{13} genome copies/ml), or AAVDJ8-
701 GFAP104-eGFP (also denoted ΔCre for simplicity; 3.98×10^{13} genome copies/ml) were made using
702 the following coordinates; X (posterior from Bregma) – 1.4 mm, Y (lateral from sagittal suture) ±
703 1.4 mm, Z (ventral from pia) – 2.1 mm. Viruses were expressed for at least 21 days (max post-
704 surgical duration of 40 days) before mice were used in physiology or imaging experiments.
705
706 *Immunohistochemistry*
707 Slices prepared from GRIN1$^{flx/flx}$ mice expressing GFAP104-nls-mCherry-Cre were fixed in 4%
708 paraformaldehyde (PFA) in 0.1 M phosphate buffer solution (PB) for 1-2 h, then washed in PB and

709 stored overnight. Alternatively, mice brain tissue was fixed with 4% PFA in PB (pH7.5) by
710 transcardial perfusion, followed by further overnight incubation of the removed brain. Fixed
711 brains were cryosectioned to a thickness of 40 µm. Slices were permeabilized with 0.3% Triton X-
712 100 and blocked in 10% goat serum, then incubated in primary antibody overnight at 4°C. Slices
713 were washed and incubated in secondary antibodies for 1-2 h at room temperature. Slices were
714 then washed and mounted in ProLong antifade mounting medium (ThermoFischer Scientific)
715 containing DAPI (1:1000, ThermoFisher Scientific), and visualized on a Zeiss 780, or an Olympus
716 FV1200 or FV3000 confocal microscope. The primary antibodies used were chicken anti-RFP (1:
717 1000, Rockland #600-901-379), mouse anti-GFAP (1:1000, Synaptic Systems #173011), rabbit
718 anti-GFAP (1:500, Abcam ab48050), rabbit anti-NeuN (1:500, Abcam #ab177487), and guinea pig
719 anti-GluN1 (1:100, Alamone Labs AGP-046). The secondary antibodies used were AlexaFluor555
720 goat anti-chicken (1:1000, Invitrogen #A32932), AlexaFluor633 goat anti-mouse (1:1000,
721 Invitrogen #A21052), AlexaFluor 488 goat anti-rabbit (1:1000, Invitrogen #A11034), AlexaFluor
722 488 goat anti-rabbit (1:500, ThermoFischer Scientific), and AlexaFluor 647 goat anti-guinea pig
723 (1:200, Invitrogen A21450).
724
725 *NMDA Receptor immunoprecipitation from mouse brain*
726 Mouse hippocampal tissues were dissociated using a glass dounce homogenizer in a 50 mM Tris-
727 HCl, pH 9.0 buffer containing protease inhibitors (10% w/v, cOmplete™, Merck). Subsequently,
728 1% (w/v) sodium deoxycholate was added and incubated for 30 min at 37°C with mild shaking to
729 solubilize the tissue. Samples were centrifuged at 100,000 rpm at 4°C for 1h. Supernatant was
730 collected, protein concentration was measured by the BCA assay, and stored at -80°C for later
731 analysis or diluted 5-fold in a 50 mM Tris-HCl pH 7.5 buffer containing 0.1% of Triton X-100 for
732 co-immunoprecipitation experiments.
733 To test for co-immunoprecipitation, a mix of Sepharose Fast-Flow protein A and protein G
734 beads was prepared. For each antibody reaction, 40 µl of the mixed resin was incubated with 5 µg
735 of antibody. After at least 2 h of incubation at 4°C excess antibody was removed by washing, and
736 2 mg of protein extract was added to each sample containing the resin beads bound by the
737 antibody and incubated overnight at 4°C. Resins were washed 3 times with 10 volumes of 50 mM
738 Tris-HCl pH 7.5 with 0.1% Triton X-100. Supernatant was carefully removed, and resins were
739 suspended in 2x SDS-PAGE protein loading buffer containing DTT. The unbound protein extract
740 was treated for a second overnight incubation at 4°C with a freshly prepared antibody-bound
741 resin under identical conditions as the first overnight incubation, to ensure effective pull-down of
742 soluble NMDA receptor content from the extract. Co-immunoprecipitated proteins from the two
743 rounds of incubation were pooled together.

Protein samples (inputs and co-immunoprecipitated proteins) were heat denatured for 2 min at 95°C, and subjected to 6% SDS-PAGE separation followed by western blot. Antibodies used were: mouse anti-NR1 (Synaptic Systems #114011), rabbit anti-GluN2A/2B (Synaptic Systems #244003), rabbit anti-GluN2C (generously provided by Dr. Masahiko Watanabe or purchased from Frontier Institute #GLURE3C-RB-AF270), mouse anti-Cre (Merck Millipore clone 2D8) and mouse anti-BirA (Novus biologicals #NBP2-59939).

Mathematical Model for the Numerical Investigation

We used the facilitation model based on the Tsodyks-Pawelzik-Markram model (Tsodyks et al., 1998) to reproduce ratios of peaks of excitatory postsynaptic current (EPSC) with a 20-Hz spike input. The synaptic dynamics is modeled by [1]:

$$\frac{dx_0(t)}{dt} = \frac{x_2(t)}{\tau_{rec}} - u_0(t_{sp}^+)x_0(t_{sp}^-)\delta(t - t_{sp}) \tag{1}$$

$$\frac{dx_1(t)}{dt} = -\frac{x_1(t)}{\tau_{in}} + u_0(t_{sp}^+)x_0(t_{sp}^-)\delta(t - t_{sp}) \tag{2}$$

$$\frac{dx_2(t)}{dt} = \frac{x_1(t)}{\tau_{in}} - \frac{x_2(t)}{\tau_{rec}} \tag{3}$$

$$\frac{du_0(t)}{dt} = -\frac{u_0(t)}{\tau_f} + U_{SE}\left(1 - u_0(t_{sp}^-)\right)\delta(t - t_{sp}). \tag{4}$$

Here x_0 is the portion of available neurotransmitters, $x_1(t)$ is the portion of neurotransmitters released by pre-synaptic spikes, $x_2(t)$ is the portion of neurotransmitters being recovered, $u_0(t)$ is the utilization of available neurotransmitters after each spike. τ_{in} is the timescale of neurotransmitters release. τ_{rec} is the recovery timescale. τ_f is the timescale of synaptic facilitation. U_{SE} is the initial release probability without the influence of synaptic facilitation. In this model, the dynamical variables are x_i with $x_0 + x_1 + x_2 = 1$.

There are four parameters to be determined: τ_f, τ_{rec}, U_{SE} and $w(0)$, where $w(0)$ is the initial connection weight between neurons. For simplicity, $w(0)$ is evenly distributed among 10 synapses (Gal et al., 2017). U_{SE} is a random number drawn from a log-normal distribution, in which the distribution is given by

$$P(U_{SE}) = \frac{1}{U_{SE}\sigma\sqrt{2\pi}}\exp\left[-\frac{(\ln|U_{SE}| - \mu)^2}{2{\sigma_{max}}^2}\right] \tag{5}$$

$$\sigma_{max} = \frac{-2 + \sqrt{4 - 4\ln|U_{max}|}}{2a} \tag{6}$$

$$\mu = \ln|U_{max}| + {\sigma_{max}}^2. \tag{7}$$

The distribution of release probability in current work was taken from Murthy et al. (1997), which was denoted by U_{SE}. In simulations we use a long-normal function to model the distribution (cf. Figure 3A).

To compare with experimental result, the excitatory postsynaptic current (EPSC) was defined as $I(t) = w(0)x_1(t)$. The best fit to the experimental data is shown in Figure S8A where the best-fit parameters are τ_f = 540 ms, τ_{rec} = 20 ms, U_{max} = 0.1 and $w(0)$ = 332.

The BCM-like learning rule for investigation is given by

$$I(t) = w(t)x_1(t) \tag{8}$$

$$\tau_w \frac{dw(t)}{dt} = I(t)[I(t) - \theta(t)^2]x_1(t) \tag{9}$$

$$\tau_\theta \frac{d\theta(t)}{dt} = \alpha I(t) - \theta(t)\,. \tag{10}$$

Here θ is the threshold to stop the change of w, while τ_θ is the timescale to integrate the postsynaptic current $I(t)$. τ_w is the timescale of $w(t)$. α is a parameter to be chosen for different scenarios: LTP or LTD. In this study, the following values were used: τ_w = 100 ms and τ_θ = 10 ms. The equations (8) to (10) constitute the BCM learning rule (Bienenstock et al., 1982).

In the series of comparisons shown in Figure 3C, the changes in synaptic plasticity as defined by

$$w\left(t = 2\text{ min}, \sigma = \frac{\sigma_{max}}{2}\right) - w(t = 2\text{ min}, \sigma = \sigma_{max}) \quad \text{for LTP} \tag{11}$$

$$w(t = 2\text{ min}, \sigma = \sigma_{max}) - w\left(t = 2\text{ min}, \sigma = \frac{\sigma_{max}}{2}\right) \quad \text{for LTD} \tag{12}$$

are represented as a function of the absolute change in the connection weight in the control release probability distribution condition as defined by $(w(t = 2\text{ min}, \sigma = \sigma_{max}) - w(t = 0))$. Note that the comparison at $t = 2$ min was to compare $w(t)$ after the epoch of paired stimulations. Note also that $\sigma = \frac{\sigma_{max}}{2}$ represents the cases of NMDARs blocked, while $\sigma = \sigma_{max}$ represents the control cases. In Figure 3C, the reduction in σ always degrades the efficacy of LTD; however, the efficacy of LTP may vary for different level of LTP. For the relative change in $w(t) \lesssim 0.06$, the reduction of σ does not degrade the LTP efficacy whereas for the relative change in $w(t) \gtrsim 0.06$, the reduction in σ degrades the LTP efficacy.

In the model and simulation based on leaky integrate-and-fire (LIF) neurons, two neurons are connected by 10 synapses. The neurons have time constant $\tau = 15$ ms, threshold potential $V_{thre} = -50.0$ mV, reversal potential $E_L = -65.0$ mV and refractory time $\tau_{ref} = 2$ ms. The rising synaptic time constant is 2 ms and decay time constant is ~5 ms. The synaptic model is the same as equations (1) – (4), and the probability distribution was the same as equations (5) – (7). The best-fit of the model to the data is shown in Figure S8B, where the parameters are τ_f = 980 ms, τ_{rec} = 25 ms, U_{max} = 0.1 and $w(0)$ = 6.7.

Statistics

All statistical analyses were performed using OriginPro software (OriginLab Corp.). Datasets were tested for normality using the Shapiro Wilk test. When the criteria for normality was achieved,

802 differences of mean values were examined using paired or unpaired Student's two-tailed t-tests
803 or one-way ANOVAs. When the criteria for normality was not achieved, differences in mean values
804 were examined using Mann-Whitney or Kruskal Wallis tests. Normalized mean values obtained
805 from recordings (i.e. normalized EPSCs) were compared to values obtained at the same timepoint
806 in control experiments using Mann-Whitney tests. Variance of PPR distributions were examined
807 using one-tailed f-tests for equal variances or Levene's test. Box plots represent median and
808 quartile values, whiskers represent maximum and minimum values that are not outliers. P values
809 are indicated throughout or indicated by * if $p<0.05$.

Acknowledgements

We would like to thank all members of the Goda laboratory for providing valuable and ongoing feedback throughout the course of this study. We thank Tatjana Tchumatchenko, Thomas Chater and Toru Shinoe for comments on the manuscript at various stages, Yun Kyung Park for help with RNA collection for RT-PCR experiments, Toru Shinoe for pilot electrophysiology experiments, Tom McHugh and Shigeyoshi Itohara for kindly providing *Grin1* floxed mice and Ai9 mice, respectively, and Masahiko Watanabe for generously providing GluN2C antibodies. PC was an Overseas Research Fellow of the Japan Society for the Promotion of Science (JSPS). This work was supported by the RIKEN Center for Brain Science, the Uehara Memorial Foundation, JSPS Core-to-Core Program (JPJSCCA20170008), Grants-in-Aid for Scientific Research (15H04280, YG; 18H05213, TF) from the MEXT, and the Brain/MINDS from the Japan AMED.

Author Contributions

PHC and YG designed the project and wrote the manuscript. PHC performed electrophysiology experiments and analyzed data. CCAF and TF contributed mathematical modeling and simulation and wrote the manuscript. PHC and AK isolated astrocyte and neuronal RNA for RT-PCR experiments. APF performed biochemistry and RT-PCR experiments. MA and KS made the GluN2C-Cre mice. APF, and AT and MK performed immunohistochemistry experiments. SGG constructed and MK prepared viral reagents.

Competing interests

The authors declare no competing interests.

References

Abbott, L.F., and Regehr, W.G. (2004). Synaptic computation. Nature *431*, 796–803.

Abe, M., Fukaya, M., Yagi, T., Mishina, M., Watanabe, M., and Sakimura, K. (2004). NMDA receptor GluRepsilon/NR2 subunits are essential for postsynaptic localization and protein stability of GluRzeta1/NR1 subunit. J. Neurosci. *24*, 7292-7304.

Alsaad, H.A., DeKorver, N.W., Mao, Z., Dravid, S.M., Arikkath, J., and Monaghan, D.T. (2019). In the Telencephalon, GluN2C NMDA Receptor Subunit mRNA is Predominately Expressed in Glial Cells and GluN2D mRNA in Interneurons. Neurochem Res. *44*, 61-77.

Amaral, D.G., and Lavenex, P. (2006). Hippocampal neuroanatomy. In The Hippocampus Book, P. Andersen, R. Morris, D. Amaral, T. Bliss, J. O'Keefe, eds. (Oxford, UK: Oxford University Press, Oxford), pp. 37-114.

Andrade-Talavera, Y., Duque-Feria, P., Paulsen, O., and Rodríguez-Moreno, A. (2016). Presynaptic Spike Timing-Dependent Long-Term Depression in the Mouse Hippocampus. Cereb

Cortex *26*, 3637-3654.

Araque, A., Carmignoto, G., Haydon, P.G., Oliet, S.H., Robitaille, R., and Volterra, A. (2014). Gliotransmitters travel in time and space. Neuron *81*, 728-739.

Attwell, D., Buchan, A.M., Charpak, S., Lauritzen, M., Macvicar, B.A., and Newman, E.A. (2010). Glial and neuronal control of brain blood flow. Nature *468*, 232–243.

Atwood, H.L., and Karunanithi, S. (2002). Diversification of synaptic strength: presynaptic elements. Nat. Rev. Neurosci. *3***,** 497–516.

Barbour, B., Brunel, N., Hakim, V., and Nadal, J.P. (2007). What can we learn from synaptic weight distributions? Trends Neurosci. *30*, 622-629.

Bazargani, N., and Attwell, D. (2016). Astrocyte calcium signaling: the third wave. Nature *19***,** 182–189.

Bender, K.J,, Allen, C.B., Bender, V.A., and Feldman, D.E. (2006). Synaptic basis for whisker deprivation-induced synaptic depression in rat somatosensory cortex. J. Neurosci. *26*, 4155-4165.

Bezaire, M.J., and Soltesz I. (2013). Quantitative assessment of CA1 local circuits: knowledge base for interneuron-pyramidal cell connectivity. Hippocampus *23*, 751-785.

Bienenstock, E.L., Cooper, L.N., and Munro, P.W. (1982). Theory for the development of neuron selectivity: orientation specificity and binocular interaction in visual cortex. J. Neurosci. *2*, 32-48.

Bindocci, E., Savtchouk, I., Liaudet, N., Becker, D., Carriero, G., and Volterra, A. (2017). Three-dimensional Ca^{2+} imaging advances understanding of astrocyte biology. Science *356*, eaai8185.

Bliss, T.V., and Collingridge, G.L. (1993). A synaptic model of memory: Long-term potentiation in the hippocampus. Nature *361*, 31–39.

Boisvert, M.M., Erikson, G.A., Shokhirev, M.N., and Allen, N.J. (2018). The Aging Astrocyte Transcriptome from Multiple Regions of the Mouse Brain. Cell Rep. *22*, 269-285.

Branco, T., Staras, K., Darcy, K.J., and Goda, Y. (2008). Local Dendritic Activity Sets Release Probability at Hippocampal Synapses. Neuron *59*, 475–485.

Branco, T., and Staras, K. (2009). The probability of neurotransmitter release: variability and feedback control at single synapses. Nat. Rev. Neurosci. *10*, 373-383.

Brenowitz, S.D., and Regehr, W.G. (2007). Reliability and Heterogeneity of Calcium Signaling at Single Presynaptic Boutons of Cerebellar Granule Cells. J. Neurosci. *27*, 7888–7898.

Bromer, C., Bartol, T.M., Bowden, J.B., Hubbard, D.D., Hanka, D.C., Gonzalez, P.V., Kuwajima, M., Mendenhall, J.M., Parker, P.H., Abraham, W.C., Sejnowski, T.J., and Harris, K.M. (2018). Long-term potentiation expands information content of hippocampal dentate gyrus synapses. Proc Natl Acad Sci. USA 115, E2410–E2418.

Brunel, N. (2016). Is cortical connectivity optimized for storing information? Nat. Neurosci. *19*, 749-755.

Burke, K.J. Jr., Keeshen, C.M., and Bender, K.J. (2018). Two Forms of Synaptic Depression Produced by Differential Neuromodulation of Presynaptic Calcium Channels. Neuron *99*, 969-984.

Buzsáki, G., and Mizuseki, K. (2014). The log-dynamic brain: how skewed distributions affect network operations. Nat. Rev. Neurosci. *15*, 264–278.

Cetin, A., Komai, S., Eliava, M., Seeburg, P.H., and Osten, P. (2007). Stereotaxic gene delivery in the rodent brain. Nat Protoc *1*, 3166–3173.

Chai, H., Diaz-Castro, B., Shigetomi, E., Monte, E., Octeau, J.C., Yu, X., Cohn, W., Rajendran, P.S., Vondriska, T.M., Whitelegge, J.P., Coppola, G., and Khakh, B.S. (2017). Neural Circuit-Specialized Astrocytes: Transcriptomic, Proteomic, Morphological, and Functional Evidence. Neuron *95*, 531–549.

Chen, J., Tan, Z., Zeng, L., Zhang, X., He, Y., Gao, W., Wu, X., Li, Y., Bu, B., Wang, W., and Duan, S. (2013). Heterosynaptic long-term depression mediated by ATP released from astrocytes. Glia *61*, 178-191.

Chung, W.S., Welsh, C.A., Barres, B.A., and Stevens, B. (2015). Do glia drive synaptic and cognitive impairment in disease? Nat Neurosci *18*, 1539-1545.

Clarke, L.E., and Barres, B.A. (2013). Emerging roles of astrocytes in neural circuit development. Nat. Rev. Neurosci. *14*, 311-321.

Collingridge, G.L., Peineau, S., Howland, J.G., and Wang, Y.T. (2010). Long-term depression in the CNS. Nat. Rev. Neurosci. 11, 459-473.

Covelo, A., and Araque, A. (2018). Neuronal activity determines distinct gliotransmitter release from a single astrocyte. Elife *7*, e32237.

Cui, Y., Yang, Y., Ni, Z., Dong, Y., Cai, G., Foncelle, A., Ma, S., Sang, K., Tang, S., Li, Y., Shen, Y., Berry, H., Wu, S., and Hu, H. (2018). Astroglial Kir4.1 in the lateral habenula drives neuronal bursts in depression. Nature *554*, 323-327.

Dallérac, G., Zapata, J., and Rouach, N. (2018). Versatile control of synaptic circuits by astrocytes: where, when and how? Nat. Rev. Neurosci. *19*, 729-743.

Deemyad, T., Lüthi, J., and Spruston, N. (2018). Astrocytes integrate and drive action potential firing in inhibitory subnetworks. Nat. Commun. *9*, 4336.

Di Castro, M.A., Chuquet, J., Liaudet, N., Bhaukaurally, K., Santello, M., Bouvier, D., Tiret, P., and Volterra, A. (2011) Local Ca^{2+} detection and modulation of synaptic release by astrocytes. Nat. Neurosci. *14*, 1276–1284.

Dobrunz, L.E., and Stevens, C.F. (1997). Heterogeneity of release probability, facilitation, and depletion at central synapses. Neuron *18*, 995–1008.

Dore, K., Stein, I.S., Brock, J.A., Castillo, P.E., Zito, K., and Sjöström, P.J. (2017). Unconventional NMDA Receptor Signaling. J. Neurosci. *37*, 10800–10807.

Éltes, T., Kirizs, T., Nusser, Z., and Holderith, N. (2017). Target cell type-dependent differences in Ca2+ channel function underlie distinct release probabilities at hippocampal glutamatergic terminals. J. Neurosci. *37*, 1910–1924.

Feldman, D.E., and Brecht, M. (2005). Map plasticity in somatosensory cortex. Science *310*, 810-815.

Fischer, G., Mutel, V., Trube, G., Malherbe, P., Kew, J.N., Mohacsi, E., Heitz, M.P., and Kemp, J.A . (1997). Ro 25-6981, a highly potent and selective blocker of N-methyl-D-aspartate receptors containing the NR2B subunit. Characterization in vitro. J. Pharmacol. Exp. Ther. *283*, 1285–1292.

Fukaya, M., Kato, A., Lovett, C., Tonegawa, S., and Watanabe, M. (2003). Retention of NMDA receptor NR2 subunits in the lumen of endoplasmic reticulum in targeted NR1 knockout mice. Proc. Natl. Acad. Sci. USA *100*, 4855–4860.

Fulterer, A., Andlauer, T.F.M., Ender, A., Maglione, M., Eyring, K., Woitkuhn, J., Lehmann, M., Matkovic-Rachid, T., Geiger, J.R.P., Walter, A.M., Nagel, K.I., and Sigrist, S.J. (2018). Active Zone Scaffold Protein Ratios Tune Functional Diversity across Brain Synapses. Cell Reports *23*, 1259–1274.

Fuzik, J., Zeisel, A., Máté, Z., Calvigioni, D., Yanagawa, Y., Szabó, G., Linnarsson, S., and Harkany, T. (2015). Integration of electrophysiological recordings with single-cell RNA-seq data identifies neuronal subtypes. Nat. Biotechnol. *34*, 175–183.

Gal, E., London, M., Globerson, A., Ramaswamy, S., Reimann, M.W., Muller, E., Markram, H., and Segev, I. (2017). Rich cell-type-specific network topology in neo-cortical microcircuitry. Nat. Neurosci. *20*, 1004-1013.

Gasparini, F., Lingenhöhl, K., Stoehr, N., Flor, P.J., Heinrich, M., Vranesic, I., Biollaz, M., Allgeier, H., Heckendorn, R., Urwyler, S., Varney, M.A., Johnson, E.C., Hess, S.D., Rao, S.P., Sacaan, A.I., Santori, E.M., Veliçelebi, G., and Kuhn, R. (1999). 2-Methyl-6-(phenylethynyl)-pyridine (MPEP), a potent, selective and systemically active mGlu5 receptor antagonist. Neuropharmacology *38*, 1493-1503.

Giaume, C., Koulakoff, A., Roux, L., Holcman, D., and Rouach, N. (2010). Astroglial networks: a step further in neuroglial and gliovascularinteractions. Nat. Rev. Neurosci. *11*, 87-99.

Glebov, O.O., Jackson, R.E., Winterflood, C.M., Owen, D.M., Barker, E.A., Doherty, P., Ewers, H., and Burrone, J . (2017). Nanoscale Structural Plasticity of the Active Zone Matrix Modulates Presynaptic Function. Cell Reports *18*, 2715–2728.

Goda, Y., and Stevens, C.F. (1998). Readily releasable pool size changes associated with long term

depression. Proc. Natl. Acad. Sci. USA *95*, 1283–1288.

Gottlieb, M., and Matute, C. (1997). Expression of ionotropic glutamate receptor subunits in glial cells of the hippocampal CA1 area following transient forebrain ischemia. J Cereb Blood Flow Metab. *17*, 290-300.

Graham, W.V., Bonito-Oliva, A., and Sakmar, T.P. (2017). Update on Alzheimer's Disease Therapy and Prevention Strategies. Annu. Rev. Med. *68*, 413-430.

Gupta, S.C., Ravikrishnan, A., Liu, J., Mao, Z., Pavuluri, R., Hillman, B.G., Gandhi, P.J., Stairs, D.J., Li, M., Ugale, R.R., Monaghan, D.T., and Dravid, S.M. (2016). The NMDA receptor GluN2C subunit controls cortical excitatory-inhibitory balance, neuronal oscillations and cognitive function. Sci Rep. *6*, 38321.

Hansen, K. B., and Traynelis, S.F. (2011). Structural and mechanistic determinants of a novel site for noncompetitive inhibition of GluN2D-containing NMDA receptors. J. Neurosci. *31*, 3650–3661.

Hansen, K.B., Yi, F., Perszyk, R.E., Furukawa, H., Wollmuth, L.P., Gibb, A.J., and Traynelis, S.F. (2018). Structure, function, and allosteric modulation of NMDA receptors. J. Gen. Physiol. *150*, 1081-1105.

Hansen, K.B., Yi, F., Perszyk, R.E., Menniti, F.S., and Traynelis, S.F. (2017). NMDA Receptors in the Central Nervous System. Methods Mol. Biol. *1677*, 1-80.

Hillman, B.G., Gupta, S.C., Stairs, D.J., Buonanno, A., Dravid, S.M. (2011). Behavioral analysis of NR2C knockout mouse reveals deficit in acquisition of conditioned fear and working memory. Neurobiol Learn Mem. *95*, 404-414.

Holderith, N., Lorincz, A., Katona, G., Rózsa, B., Kulik, A., Watanabe, M., and Nusser, Z. (2012). Release probability of hippocampal glutamatergic terminals scales with the size of the active zone. Nat. Neurosci. *15*, 988–997.

Jourdain, P., Bergersen, L.H., Bhaukaurally, K., Bezzi, P., Santello, M., Domercq, M., Matute, C., Tonello, F., Gundersen, V., and Volterra, A. (2007). Glutamate exocytosis from astrocytes controls synaptic strength. Nat. Neurosci. *10*, 331–339.

Káradóttir, R., Cavelier, P., Bergersen, L.H., and Attwell, D. (2005). NMDA receptors are expressed in oligodendrocytes and activated in ischaemia. Nature *438*, 1162-1166.

Karavanova, I., Vasudevan, K., Cheng, J., and Buonanno, A. (2007). Novel regional and developmental NMDA receptor expression patterns uncovered in NR2C subunit-β-galactosidase knock-in mice. Molecular and Cellular Neuroscience *34*, 468–480.

Khakh, B.S., and Sofroniew, M.V. (2015). Diversity of astrocyte functions and phenotypes in neural circuits. Nat. Neurosci. *18*, 942–952.

Kirchhoff, F. (2017) Analysis of Functional NMDA Receptors in Astrocytes. Methods Mol Biol *1677*, 241-251.

Kotermanski, S.E., and Johnson, J.W. (2009). Mg^{2+} imparts NMDA receptor subtype selectivity to the Alzheimer's drug memantine. J. Neurosci. *29*, 2774-2779.

Krebs, C., Fernandes, H.B., Sheldon, C., Raymond, L.A., and Baimbridge, K.G. (2003) Functional NMDA receptor subtype 2B is expressed in astrocytes after ischemia in vivo and anoxia in vitro. J. Neurosci. *23*, 3364–3372.

Krystal, J.H., Abdallah, C.G., Sanacora, G., Charney, D.S., and Duman, R.S. (2019). Ketamine: A Paradigm Shift for Depression Research and Treatment. Neuron *101*, 774-778.

Lalo, U., Pankratov, Y., Kirchhoff, F., North, R.A., and Verkhratsky, A. (2006). NMDA receptors mediate neuron-to-glia signaling in mouse cortical astrocytes. Journal of Neuroscience *26*, 2673–2683.

Lanjakornsiripan, D., Pior, B.J., Kawaguchi, D., Furutachi, S., Tahara, T., Katsuyama, Y., Suzuki, Y., Fukazawa, Y., and Gotoh, Y. (2018). Layer-specific morphological and molecular differences in neocortical astrocytes and their dependence on neuronal layers. Nat. Commun. *9*, 1623.

Larkman, A., Hannay, T., Stratford, K., and Jack, J. (1992). Presynaptic release probability influences the locus of long-term potentiation. Nature *360*, 70–73.

Letellier, M. Park, Y.K., Chater, T.E., Chipman, P.H., Gautam, S.G., Oshima-Takago, T., and Goda, Y. (2016). Astrocytes regulate heterogeneity of presynaptic strengths in hippocampal networks. Proc. Natl. Acad. Sci. USA *113*, E2685-94.

Lines, J., Covelo, A., Gómez, R., Liu, L., and Araque, A. (2017). Synapse-specific regulation revealed at single synapses is concealed when recording multiple synapses. Front. Cell. Neurosci. *11*:367.

Madisen, L., Zwingman, T.A., Sunkin, S.M., Oh, S.W., Zariwala, H.A., Gu, H., Ng, L.L., Palmiter, R.D., Hawrylycz, M.J., Jones, A.R., Lein, E.S., and Zeng, H. (2010). A robust and high-throughput Cre reporting and characterization system for the whole mouse brain. Nat Neurosci. *13*, 133-140.

Malenka RC, Bear MF. (2004). LTP and LTD: an embarrassment of riches. Neuron *44*, 5-21.

Malinow, R., and Tsien, R.W. (1990). Presynaptic enhancement shown by whole-cell recordings of long-term potentiation in hippocampal slices. Nature *346*, 177–180.

Mao, Z., Mao, Z., He, S., Mesnard, C., Synowicki, P., Zhang, Y., Chung, L., Wiesman, A.I., Wilson, T.W., and Monaghan, D.T. (2020). NMDA receptors containing GluN2C and GluN2D subunits have opposing roles in modulating neuronal oscillations; potential mechanism for bidirectional feedback. Brain Res. *1727*, 146571.

Markram, H., and Sakmann, B. (1995). Action potentials propagating back into dendrites triggers changes in efficacy. Society of Neuroscience Abstract. 21.

Markram, H., Wang, Y., and Tsodyks, M. (1998). Differential signaling via the same axon of

neocortical pyramidal neurons. Proc. Natl. Acad. Sci. USA *95*, 5323–5328.

Marra, V., Burden, J.J., Thorpe, J.R., Smith, I.T., Smith, S.L., Häusser, M., Branco, T., and Staras, K. (2012). A Preferentially Segregated Recycling Vesicle Pool of Limited Size Supports Neurotransmission in Native Central Synapses. Neuron *76*, 579-589.

Martín, R., Bajo-Grañeras, R., Moratalla, R., Perea, G., and Araque, A. (2015). Circuit-specific signaling in astrocyte-neuron networks in basal ganglia pathways. Science *349*, 730–734.

Martin-Fernandez, M., Jamison, S., Robin, L.M., Zhao, Z., Martin, E.D., Aguilar, J., Benneyworth, M.A., Marsicano, G., and Araque, A. (2017). Synapse-specific astrocyte gating of amygdala-related behavior. Nat. Neurosci. *20*, 1540–1548.

Matz, J., Gilyan, A., Kolar, A., McCarvill, T, and Krueger, S.R. (2010). Rapid structural alterations of the active zone lead to sustained changes in neurotransmitter release. Proc. Natl. Acad. Sci. USA. *107*, 8836-8841.

Miyazaki, T., Yamasaki, M., Hashimoto, K., Yamazaki, M., Abe, M., Usui, H., Kano, M., Sakimura, K., and Watanabe, M. (2012). Cav2.1 in cerebellar Purkinje cells regulates competitive excitatory synaptic wiring, cell survival, and cerebellar biochemical compartmentalization. J Neurosci. *32*, 1311-1328.

Murthy, V.N., Sejnowski, T.J., and Stevens, C.F. (1997). Heterogeneous release properties of visualized individual hippocampal synapses. Neuron *18*, 599-612.

Murphy-Royal, C., Dupuis, J.P., Varela, J.A., Panatier, A., Pinson, B., Baufreton, J., Groc, L., and Oliet, S.H. (2015). Surface diffusion of astrocytic glutamate transporters shapes synaptic transmission. Nat. Neurosci. *18*, 219–226.

Navarrete, M., Cuartero, M.I., Palenzuela, R., Draffin, J.E., Konomi, A., Serra, I., Colié, S., Castaño-Castaño, S., Hasan, M.T., Nebreda, Á.R., and Esteban, J.A. (2019). Astrocytic p38α MAPK drives NMDA receptor-dependent long-term depression and modulates long-term memory. Nat. Commun. *10*, 2968.

Nicoll, R.A. (2017). A brief history of long-term potentiation. Neuron *93*, 281-290.

Nimmerjahn, A., Kirchhoff, F., Kerr, J.N., and Helmchen, F. (2004). Sulforhodamine 101 as a specific marker of astroglia in the neocortex in vivo. Nat. Methods *1*, 31-37.

Paoletti, P., Bellone, C., and Zhou, Q. (2013). NMDA receptor subunit diversity: impact on receptor properties, synaptic plasticity and disease. Nat. Rev. Neurosci. *14*, 383-400.

Panatier, A., Vallée, J., Haber, M., Murai, K.K., Lacaille, J.C., and Robitaille, R. (2011). Astrocytes Are Endogenous Regulators of Basal Transmission at Central Synapses. Cell *146*, 785–798.

Pannasch, U., Freche, D., Dallérac, G., Ghézali, G., Escartin, C., Ezan, P., Cohen-Salmon, M., Benchenane, K., Abudara, V., Dufour, A., Lübke, J.H., Déglon, N., Knott, G., Holcman,

D., and Rouach, N. (2014). Connexin 30 sets synaptic strength by controlling astroglial synapse invasion. Nat. Neurosci. *17*, 549–558.

Park, H., Li, Y., and Tsien, R.W. (2012). Influence of Synaptic Vesicle Position on Release Probability and Exocytotic Fusion Mode. Science *335*, 1362–1366.

Pascual, O., Casper, K.B., Kubera, C., Zhang, J., Revilla-Sanchez, R., Sul, J.Y., Takano, H., Moss, S.J., McCarthy, K., and Haydon, P.G. (2005). Astrocytic Purinergic Signaling Coordinates Synaptic Networks. Science *310*, 113–116.

Perea, G., and Araque, A. (2007). Astrocytes Potentiate Transmitter Release at Single Hippocampal Synapses. Science *317*, 1083–1086.

Pinto-Duarte, A., Roberts, A.J., Ouyang, K., and Sejnowski, T.J. (2019). Impairments in remote memory caused by the lack of Type 2 IP_3 receptors. Glia *67*, 1976-1989.

Ravikrishnan, A., Gandhi, P.J., Shelkar, G.P., Liu, J., Pavuluri, R., and Dravid, S.M. (2018). Region-specific Expression of NMDA Receptor GluN2C Subunit in Parvalbumin-Positive Neurons and Astrocytes: Analysis of GluN2C Expression using a Novel Reporter Model. Neurosci. *380*, 49–62.

Reyes, A., Lujan, R., Rozov, A., Burnashev, N., Somogyi, P., and Sakmann, B. (1998). Target-cell-specific facilitation and depression in neocortical circuits. Nat. Neurosci. *1*, 279–285.

Rotman, Z., and Klyachko, V.A. (2013). Role of synaptic dynamics and heterogeneity in neuronal learning of temporal code. J. Neurophysiol. *110*, 2275–2286.

Royer, S., and Paré, D. (2003). Conservation of total synaptic weight through balanced synaptic depression and potentiation. Nature *422*, 518-522.

Saab, A.S., Tzvetavona, I.D., Trevisiol, A., Baltan, S., Dibaj, P., Kusch, K., Möbius, W., Goetze, B., Jahn, H.M., Huang, W., Steffens, H., Schomburg, E.D., Pérez-Samartín, A., Pérez-Cerdá, F., Bakhtiari, D., Matute, C., Löwel, S., Griesinger, C., Hirrlinger, J., Kirchhoff, F., and Nave, K.A. (2016). Oligodendroglial NMDA Receptors Regulate Glucose Import and Axonal Energy Metabolism. Neuron *91*, 119-132.

Sakers, K., Lake, A.M., Khazanchi, R., Ouwenga, R., Vasek, M.J., Dani, A., and Dougherty, J.D. (2017). Astrocytes locally translate transcripts in their peripheral processes. Proc. Natl. Acad. Sci. USA *114*, E3830-E3838.

Santello, M., Toni, N., and Volterra, A. (2019). Astrocyte function from information processing to cognition and cognitive impairment. Nat Neurosci. *22*, 154-166.

Sanz-Clemente, A., Nicoll, R.A., and Roche, K.W. (2013). Diversity in NMDA receptor composition: many regulators, many consequences. Neuroscientist *19*, 62-75.

Schipke, C.G., Ohlemeyer, C., Matyash, M., Nolte, C., Kettenmann, H., and Kirchhoff, F. (2001). Astrocytes of the mouse neocortex express functional N-methyl-D-aspartate

receptors. FASEB J *15*, 1270-1272.

Schroeder, A., Vanderlinden, J., Vints, K., Ribeiro, L.F., Vennekens, K.M., Gounko, N.V., Wierda, K.D., and de Wit, J. (2018). A Modular Organization of LRR Protein-Mediated Synaptic Adhesion Defines Synapse Identity. Neuron *99*, 329-344.

Schwarz, Y., Zhao, N., Kirchhoff, F., and Bruns, D. (2017). Astrocytes control synaptic strength by two distinct v-SNARE-dependent release pathways. Nat. Neurosci. *20*, 1529-1539.

Serrano, A., Robitaille, R., and Lacaille, J.-C. (2008). Differential NMDA-dependent activation of glial cells in mouse hippocampus. Glia *56*, 1648–1663.

Shih, P.-Y., Savtchenko, L.P., Kamasawa, N., Dembitskaya, Y., McHugh, T.J., Rusakov, D.A., Shigemoto, R., and Semyanov, A. (2013). Retrograde Synaptic Signaling Mediated by K+ Efflux through Postsynaptic NMDA Receptors. Cell Rep. *5*, 941–951.

Simard, M., and Nedergaard, M. (2004). The neurobiology of glia in the context of water and ion homeostasis. Neuroscience *129*, 877–896.

Sun, W., McConnell, E., Pare, J.F., Xu, Q., Chen, M., Peng, W., Lovatt, D., Han, X., Smith, Y., and Nedergaard, M. (2013). Glutamate-dependent neuroglial calcium signaling differs between young and adult brain. Science *339*, 197–200.

Tan, Z., Liu, Y., Xi, W., Lou, H.F., Zhu, L., Guo, Z., Mei, L., and Duan, S. (2017). Glia-derived ATP inversely regulates excitability of pyramidal and CCK-positive neurons. Nat. Commun. *8*, 13772.

Thalhammer, A., Contestabile, A., Ermolyuk, Y.S., Ng, T., Volynski, K.E., Soong, T.W., Goda, Y., and Cingolani, L.A. (2017). Alternative Splicing of P/Q-Type Ca^{2+} Channels Shapes Presynaptic Plasticity. Cell Rep. *20*, 333–343.

Tsodyks, M., Pawelzik, K., and Markram, H. (1998). Neural networks with dynamic synapses. Neural Comput. *10*, 821-835.

Turrigiano, G.G. (2017). The dialectic of Hebb and homeostasis. Philos. Trans. R. Soc. Lond. B Biol. Sci. *372*, pii: 20160258.

Vitureira, N., and Goda, Y. (2013). Cell biology in neuroscience: the interplay between Hebbian and homeostatic synaptic plasticity. J. Cell Biol. *203*, 175-186.

Watanabe, M., Inoue, Y., Sakimura, K., Mishina, M. (1993). Distinct distributions of five N-methyl-D-aspartate receptor channel subunit mRNAs in the forebrain. J. Comp. Neurol. *338*, 377-390.

Williams, N.R., and Schatzberg, A.F. (2016). NMDA antagonist treatment of depression. Curr. Opin. Neurobiol. *36*, 112-117.

Zenke, F., and Gerstner, W. (2017). Hebbian plasticity requires compensatory processes on multiple timescales. Philos. Trans. R. Soc. Lond. B Biol. Sci. *372*, pii: 20160259.

Zhang, J.-M., Wang, H.K., Ye, C.Q., Ge, W., Chen, Y., Jiang, Z.L., Wu, C.P., Poo, M.M., and Duan, S.

(2003). ATP released by astrocytes mediates glutamatergic activity-dependent heterosynaptic suppression. Neuron *40*, 971–982.

Zhang, Y., Chen, K., Sloan, S.A., Bennett, M.L., Scholze, A.R., O'Keeffe, S., Phatnani, H.P., Guarnieri, P., Caneda, C., Ruderisch, N., Deng, S., Liddelow, S.A., Zhang, C., Daneman, R., Maniatis, T., Barres, B.A., and Wu, J.Q. (2014). An RNA-sequencing transcriptome and splicing database of glia, neurons, and vascular cells of the cerebral cortex. J. Neurosci. *34*, 11929–11947.

Zhang, Y., and Barres, B.A. (2010). Astrocyte heterogeneity: an underappreciated topic in neurobiology. Curr. Opin. Neurobiol. *20*, 588–594.

Zuchero, J.B., and Barres, B.A. (2015). Glia in mammalian development and disease. Development *142*, 3805-3809.

Main Figures

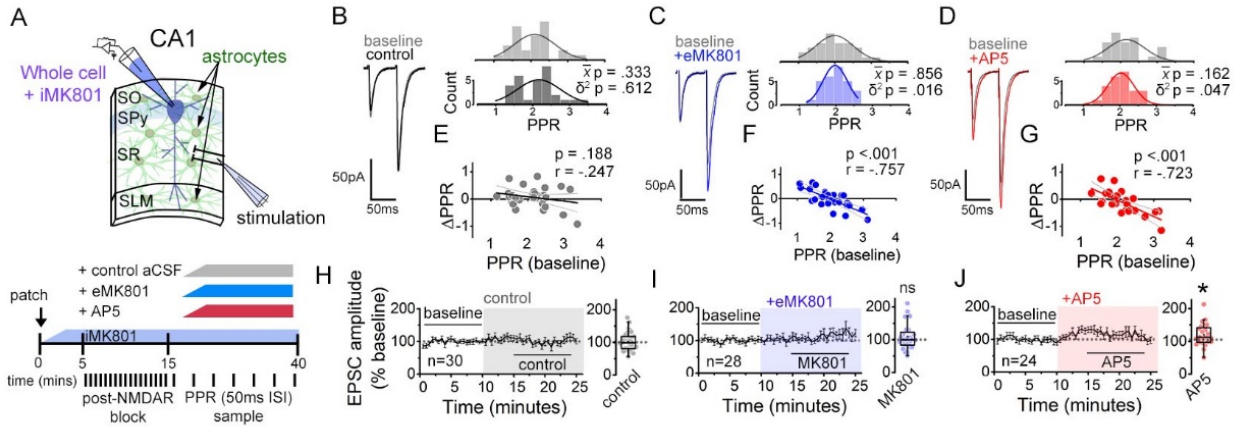

Figure 1. Astrocyte NMDARs contribute to synaptic strength diversity of Schaffer collateral synapses. (**A**) Experimental scheme for assessing the functional role of non-postsynaptic NMDARs in synaptic transmission. MK801 was included in the patch pipette to perfuse the CA1 pyramidal neuron for 10-15 min (top), and pairs of stimuli (Δt = 50 ms) were applied at 0.1Hz for at least 45 time to pre-block postsynaptic NMDARs in prior to bath applying NMDAR antagonists (see bottom). (**B-D**) Representative EPSC traces (average of 20 sweeps) to pairs of pulses (Δt = 50 ms) applied to Schaffer collateral axons before (baseline) and after wash-on of control aCSF (control) (*B*), MK801 (50 μM) (*C*), or AP5 (50 μM) (*D*). (**E-G**) Scatterplots of the change in PPR vs. the initial PPR in control aCSF (*E*), MK801 (*F*), or AP5 (*G*) where ΔPPR = $PPR_{experimental}$-$PPR_{baseline}$. Linear fits, Pearson's correlation coefficients (r) and p values are shown. X intercept, MK801 = 1.97, AP5 = 1.95. (**H-J**) Plots of EPSC amplitudes (normalized to the baseline average) before and during the application of NMDAR antagonists (shaded area) where n is the number of inputs examined for each experiment. Baseline and experimental periods are indicated (black bars). Box plots to the right show the summary of normalized EPSC amplitudes during the application of indicated inhibitors. Histograms of the distribution of PPRs recorded during the baseline (*light grey*) and control aCSF/drug application periods (*shaded area*) were fit with single Gaussian curves. The p values for the comparison of the baseline to the experimental periods for the population mean ($\bar{x}$) and variance (δ^2) were obtained by two-tailed paired sample t-test and one-tailed f-test for equal variances, respectively. * p<0.05 Mann-Whitney U-test were used to compare the experimental control condition to the experimental drug conditions. Control = 30 inputs, 15 cells, 13 mice; MK801 = 28 inputs, 14 cells, 9 mice; AP5 = 24 inputs, 12 cells, 11 mice.

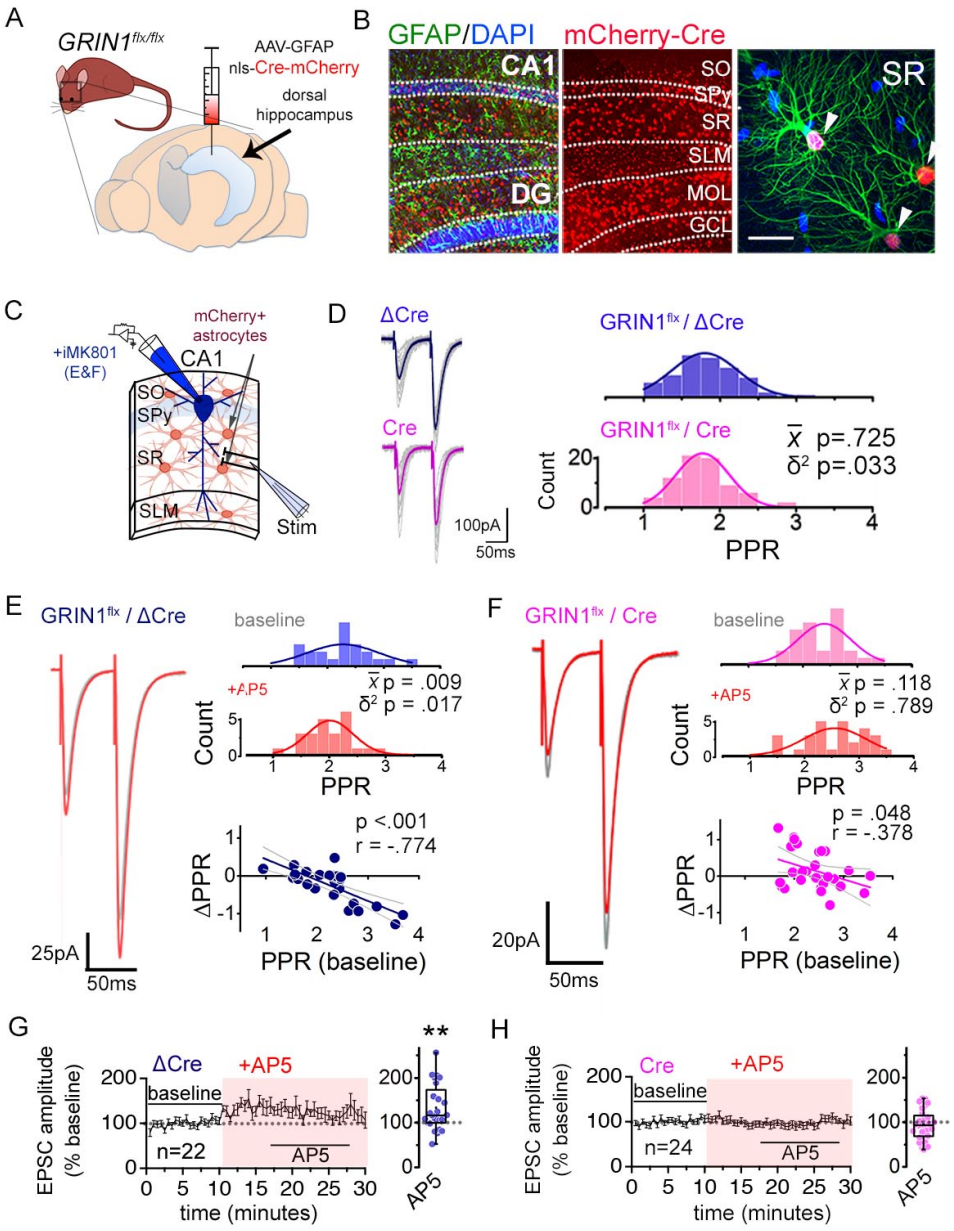

Figure 2. The reduction of synaptic strength diversity by the NMDAR antagonists requires astrocyte NMDARs. (**A**) Experimental scheme: AAV-GFAP104-nls-mCherry-Cre (Cre) or AAV-GFAP104-nls-mCherry (ΔCre) was injected into the dorsal hippocampus of adult GRIN1$^{flx/flx}$ mice to conditionally knock-down GluN1 in astrocytes. (**B**) Representative maximum intensity projection confocal image showing the CA1 region of a mouse hippocampal section prepared 21 days after injecting the AAV-GFAP104-
nls-mCherry-Cre virus and immunolabelled against GFAP (green) and mCherry (red) and stained with DAPI (blue). SO, *stratum oriens*; SPy, *stratum pyramidale*; SR, *stratum radiatum*; SLM, *stratum lacunosum moleculare*; MOL, molecular layer; GCL, granule cell layer. Magnified view (right panel) of a region in SR shows highly restricted expression of mCherry to GFAP-positive astrocytes (arrowheads). Scale bar 20 µm. (**C**) Recording configuration: CA1 pyramidal neurons were patched in acute hippocampal slices prepared 21 days after ΔCre or Cre AAV infection. EPSCs were elicited by placing the stimulating electrode in the SR. MK801 was included in the patch pipette for experiments in panels *E-H*. (**D**) Left: Averaged EPSC traces from representative recordings in SR in slices from control ΔCre (top) or Cre (bottom) virus-infected mice. Individual traces are

shown in grey. Right: Histograms of the distribution of PPRs recorded in the SR of ΔCre (top) and Cre slices (bottom) were fit with single Gaussians. The p values shown were obtained for the population mean ($\bar{x}$) (two-tailed t-test) and variance (δ^2) (one-tailed f-test for equal variances) comparing PPR distributions from ΔCre (n=72 inputs, 43 cells, 14 mice) and Cre (n=74 inputs, 46 cells, 12 mice) slices. (**E-H**) Average EPSC traces in baseline (grey) and following drug treatment (color) from a representative experiment in each condition (left); PPR histograms (top right) and ΔPPR vs. baseline PPR plots (bottom right) before (baseline) and after bath applying AP5 (50 μM) to ΔCre (*E*) and Cre (*F*) slices. The p values were obtained for the population mean ($\bar{x}$) (paired sample t-test) and variance (δ^2) (one-tailed f-test for equal variances) comparing PPRs before and after the drug treatment. Linear fits and Pearson's correlation coefficients (r) and p values are shown in scatter plots. (**G,H**) Plots of EPSC amplitudes (normalized to the baseline average) before and during the application of AP5 to ΔCre (*G*) and Cre-infected (*H*) slices (shaded area) where n is the number of inputs examined for each experiment. Baseline and experimental periods are indicated (black bars). Box plots to the right show the summary of normalized EPSC amplitudes during the application of indicated inhibitors. The p values shown were obtained for the population mean ($\bar{x}$) (two-tailed t-test) and variance (δ^2) (one-tailed f-test for equal variances) comparing PPR distributions of the experimental drug periods to the baseline period.** p = 0.005 Mann-Whitney U-test, comparing the experimental drug periods between ΔCre and Cre conditions. ΔCre +AP5 = 24 inputs, 12 cells, 5 mice; Cre +AP5 = 28 inputs, 14 cells, 5 mice.

(*Figure 2 legend continued from previous page*)

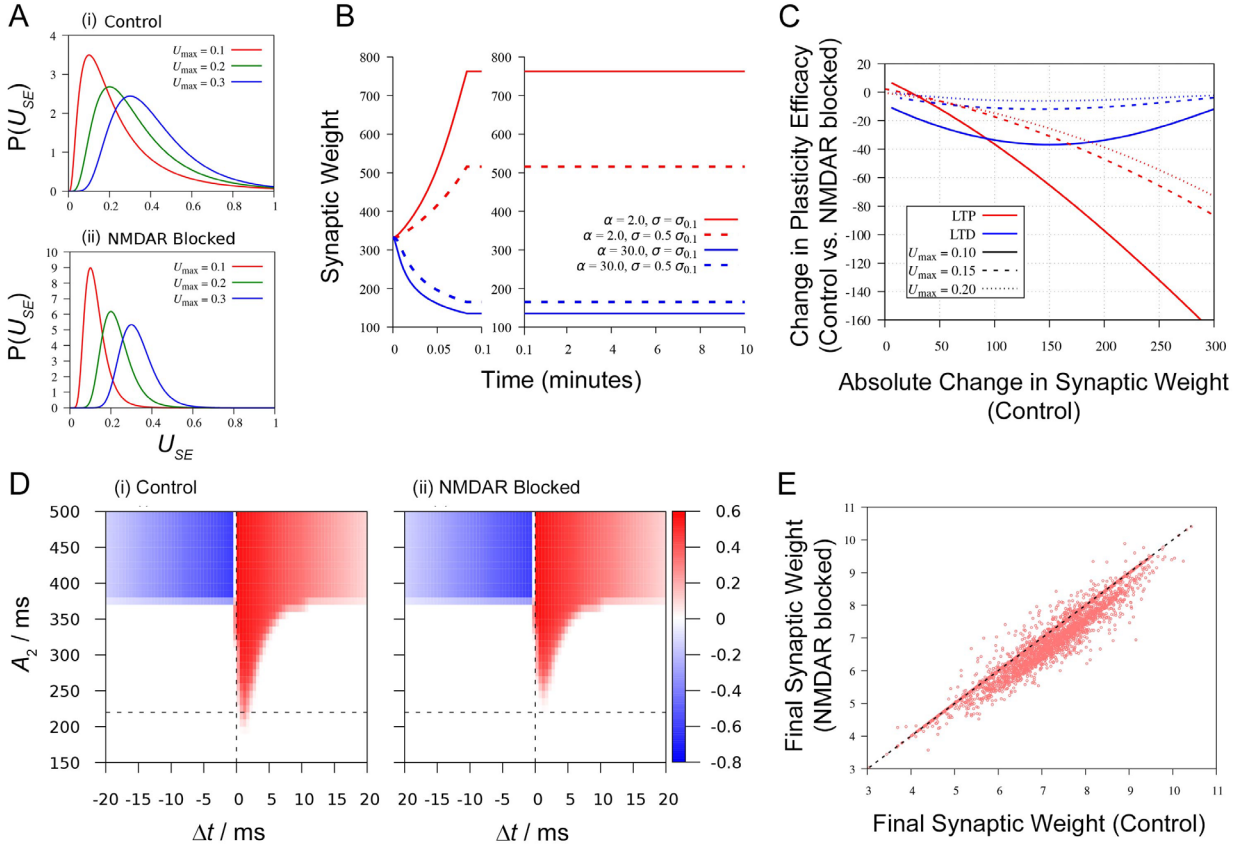

Figure 3. Synaptic strength diversity impacts long-term synaptic plasticity. (**A**) Variations of release probability distribution U_{SE}, with different peak locations (U_{max} = 0.1, red; U_{max} = 0.2, green; U_{max} = 0.3, blue) modelled using a log-normal distribution reported by Murthy et al., (1997). The plot shows release probability distributions for the control condition (i) and the condition of reduced release probability variance mimicking the NMDAR-block condition (ii). (**B**) Example results of the BCM-like learning simulation. Traces show synaptic weight function $w(t)$ for LTP (red: α = 2.0) and LTD (blue: α = 30.0) simulations where long-term synaptic plasticity is induced by applying 100 presynaptic spikes with 50 ms inter-spike intervals; the decay of synaptic plasticity has not been considered in the model. Two limiting cases of the release probability distributions of the presynaptic neuron (control, solid line; NMDAR block, dotted line; U_{max} = 0.1 for both cases) as illustrated in (*Ai*) and (*Aii*) are shown. (**C**) Plot of the difference of the synaptic weight change at w(t = 2 min) between the release probability distributions representing control and NMDAR block for LTP (red) and LTD (blue) as a function of the change in synaptic weight w(t = 2 min) for the control case over a range of potentiation or depression. The horizontal axis is defined by $w(t = 2\text{ min}, \sigma = \sigma_{max}) - w(t = 0)$. The difference of synaptic weight in the y-axis is defined as $w\left(t = 2\text{ min}, \sigma = {}^{\sigma_{max}}/_{2}\right) - w(t = 2\text{ min}, \sigma = \sigma_{max})$ for LTP and as $w(t = 2\text{ min}, \sigma = \sigma_{max}) - w\left(t = 2\text{ min}, \sigma = {}^{\sigma_{max}}/_{2}\right)$ for LTD. The relationship is shown for three different peak distributions, U_{max}, for both LTP and LTD (U_{max} = 0.1, solid line; U_{max} = 0.2, dashed line; U_{max} = 0.3, dotted line). (**D**) Simulation result using two leaky integrate-and-fire neurons. Changes in synaptic weight w(t) after giving 10 spike pairs in which the current injection to the presynaptic neuron is 500 pA and the postsynaptic neuron is A_2, in control (i) and in NMDAR blocked condition (ii). The current injection sequences to the presynaptic and the postsynaptic neurons are separated by a time difference Δt. Color intensity shows potentiation (red) and depression (blue) of synaptic weight changes. Vertical dashed line: Δt = 0. Horizontal dashed line: the least A_2 to evoke LTP under the NMDAR-block condition. (**E**) A comparison of the simulation result using Poisson spike trains. Each data point represents the synaptic weights after applying the same pair of Poisson sequences

for the release probability distribution representing the control condition (x-axis) and the NMDAR block condition (y-axis). The NMDAR block condition consistently shows smaller synaptic weight compared to the control condition.

(*Figure 3 legend continued from previous page*)

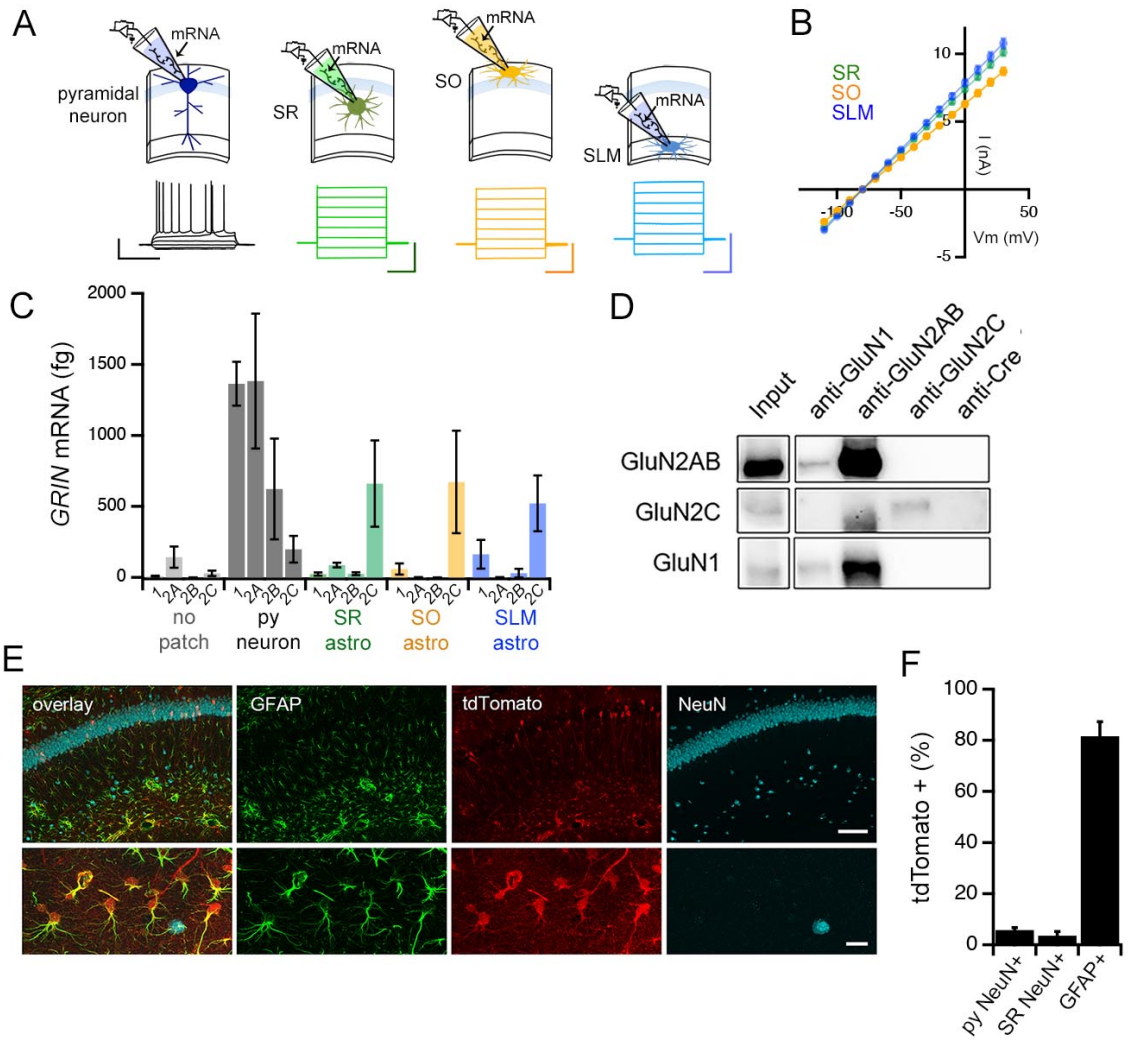

Figure 4. Astrocytes in the adult mouse hippocampus express NMDA receptors containing the GluN2C subunit. (**A**) Top row illustrates single cell RT-PCR strategy using the patch-clamp technique. Bottom row shows representative voltage responses to current steps recorded in CA1 pyramidal neuron (far left, black), and current responses to voltage steps in astrocytes in *stratum radiatum* (SR, green), *stratum oriens* (SO, yellow), and *stratum lacunosum moleculare* (SLM, blue). Scale bars: pyramidal neuron, 40 mV, 500 ms; astrocytes, 6 nA, 200 ms. (**B**) Summary of I-V curves obtained from astrocytes prior to collection of RNA. N = 39 cells, 36 slices, 9 mice for each layer. (**C**) Summary plot of RT-PCR analysis using RNA obtained by whole-cell patch clamping of area CA1 pyramidal neurons (N) and astrocytes from SR, SO, and SLM or control electrode inserted into the slice without patching cells (no patch), examined for mRNA encoding indicated NMDAR subunits: *GRIN1* (1), *GRIN2A* (2A), *GRIN2B* (2B), and *GRIN2C* (2C). See Methods for details. *GRIN2D* levels were undetectable in all cells examined (data not shown). (**D**) Western blots for co-immunoprecipitations performed using mouse hippocampal extracts with the indicated antibodies where Cre was used as a negative control: the blots are probed for GluN2A/2B (top row), GluN2C (middle row) or GluN1 (bottom row). (**E**) Representative brain sections of *GRIN2C*-Cre mice crossed to a tdTomato reporter line, showing hippocampal area CA1 immunolabelled for GFAP, tdTomato and NeuN; scale bars are 160 µm (top), 25 µm (bottom). (**F**) Quantification of the proportion (%) of NeuN-labelled cells in *stratum pyramidale* (left) and SR (middle) and GFAP-labelled cells (right) that are positive for tdTomato.

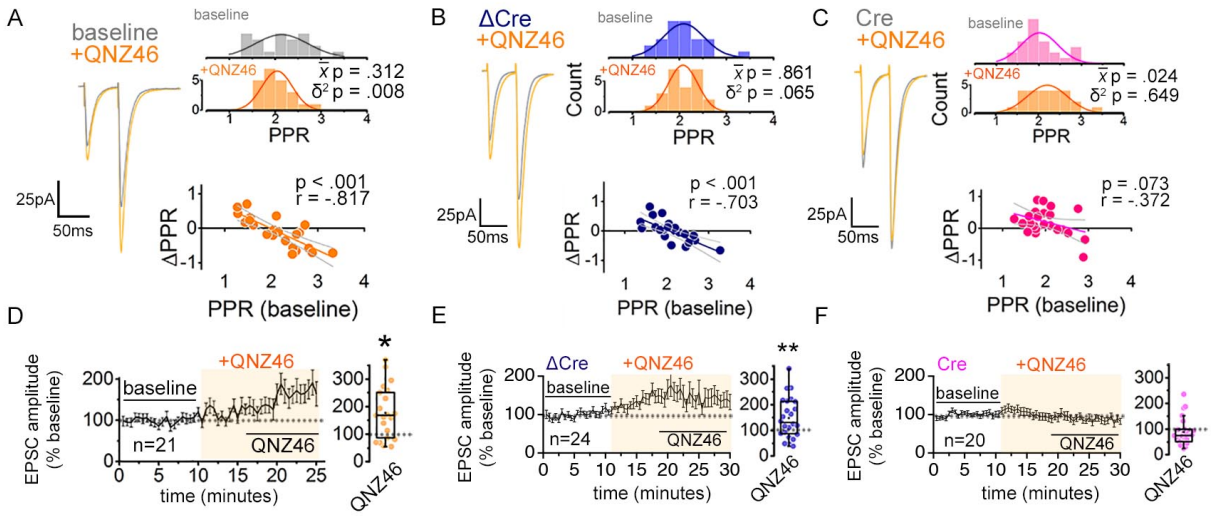

Figure 5. Inhibiting GluN2C NMDARs reduces PPR variability which is sensitive to astrocyte expression of GluN1. (**A**) Representative EPSC traces (average of 20 sweeps) to pairs of pulses (50 ms interstimulus interval) applied to Schaffer collateral axons before (baseline) and after wash-on of QNZ46 (25 μM). (**B**) Scatterplots of the change in PPR vs. the initial PPR in QNZ46 where ΔPPR = $PPR_{experimental}$-$PPR_{baseline}$. Linear fits, Pearson's correlation coefficients (r) and p values are shown. X intercept = 2.07. (**C**) Plots of EPSC amplitudes (normalized to the baseline average) before and during the application of NMDAR antagonists (shaded area) where n is the number of inputs examined for each experiment. Baseline and experimental periods are indicated (black bars). Box plots to the right show the summary of normalized EPSC amplitudes during the application of indicated inhibitors. Histograms of the distribution of PPRs recorded during the baseline (*light grey*) and control aCSF/drug application periods (*darker colors*) were fit with single Gaussian curves. The p values for the comparison of the baseline to the experimental periods for the population mean ($\bar{x}$) and variance (δ^2) were obtained by two-tailed paired sample t-test and one-tailed f-test for equal variances, respectively. * p<0.05 Mann-Whitney U-test were used to compare the experimental control condition to the experimental drug conditions. 22 inputs, 11 cells, 7 mice. (**D,E**) Average EPSC traces in baseline (grey) and following QNZ46 (25 μM) treatment (color) from a representative experiment (left); PPR histograms (top right) and ΔPPR vs. baseline PPR plots (bottom right) before (baseline) and after bath applying QNZ46 to ΔCre (*D*) and Cre (*F*) slices. The p values were obtained for the population mean ($\bar{x}$) (paired sample t-test) and variance (δ^2) (one-tailed f-test for equal variances) comparing PPRs before and after the drug treatment. Linear fits and Pearson's correlation coefficients (r) and p values are shown in scatter plots. (**F,G**) Plots of EPSC amplitudes (normalized to the baseline average) before and during the application of QNZ46 to ΔCre (*F*) and Cre-infected (*G*) slices (shaded area) where n is the number of inputs examined for each experiment. Baseline and experimental periods are indicated (black bars). Box plots show the summary of normalized EPSC amplitudes during the QNZ46 application. The p values shown were obtained for the population mean ($\bar{x}$) (two-tailed t-test) and variance (δ^2) (one-tailed f-test for equal variances) comparing PPR distributions of the QNZ46 application period to the baseline period.** p = 0.005 Mann-Whitney U-test, comparing the experimental drug periods between ΔCre and Cre conditions. ΔCre +QNZ46 = 24 inputs, 12 cells, 5 mice; Cre +QNZ46 = 24 inputs, 12 cells, 6 mice.

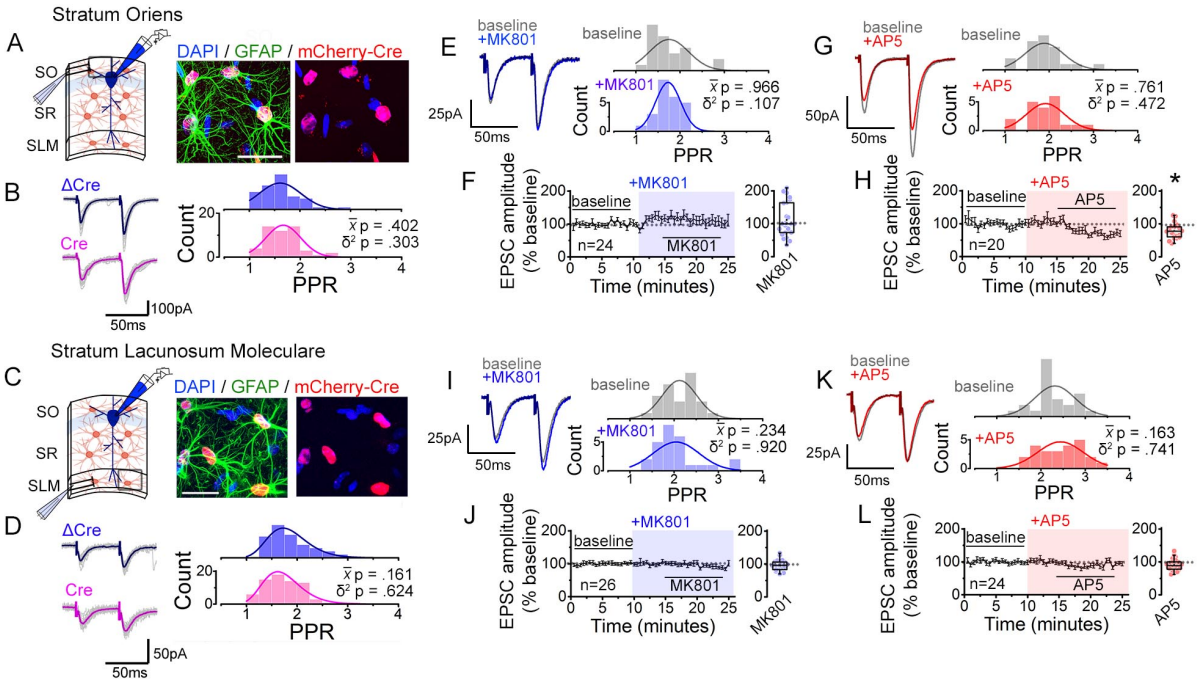

Figure 6. Interfering with astrocyte NMDARs has little effect on synaptic strength diversity in the *stratum oriens* (SO) and the *stratum lacunosum moleculare* (SLM). (**A**) Left: Illustration of stimulation configuration. Right: maximum intensity projection confocal image of a region of SO in hippocampal CA1 showing nls-mCherry-Cre-expressing astrocytes counter-stained for GFAP and DAPI. Scale bar, 20 µm. (**B**) Averaged (color) and individual (grey) EPSC sweeps from representative recordings in SO of ΔCre and Cre infected slices. Histograms of PPRs from ΔCre (top) and Cre-expressing slices (bottom) were fit with single Gaussians. The p values obtained for the population mean ($\bar{x}$) (Mann-Whitney test) and variance (δ^2) (one-tailed f-test for equal variances) comparing ΔCre to Cre PPR distributions. ΔCre, n = 50 inputs, 25 cells, 7 mice; Cre, n = 50 inputs, 25 cells, 7 mice. (**C,D**) Same analysis as shown in *A,B* for astrocytes and PPRs measured in SLM. ΔCre, n = 67 inputs, 47 cells, 12 mice; Cre, n = 71 inputs, 49 cells, 12 mice. (**E**) Representative traces of EPSCs (left) and histograms of PPRs elicited by stimulation of axons in SO recorded before (baseline) and after MK801 application. n = 24 inputs, 12 cells, 6 mice. (**F**) Time-course of EPSC amplitudes (normalized to the baseline average) before and during the application of MK801(shaded area) where the n# shown is the number of independent inputs examined. Box plots to the right show the summary of normalized EPSC amplitudes during the MK801 experimental period (black bar). (**G,H**) Same analysis as shown in *E,F* for PPRs elicited in SO during the application of AP5. n = 20 inputs, 10 cells, 7 mice. * $p<0.05$ Mann-Whitney U-test (control aCSF vs. AP5). (**I-L**) Same analysis as *E-H* for PPRs elicited in SLM with MK801 (*I,J*) and AP5 application (*K,L*). MK801, n = 26 inputs, 13 cells, 8 mice; AP5, n = 24 inputs, 12 cells, 6 mice. Histograms shown in *E-L* were fit with single Gaussian curves and the p values for the population mean ($\bar{x}$) and variance (δ^2) were assessed using two tailed, paired sample t-test and one-tailed f-test for equal variances, respectively.

Supplementary Figures

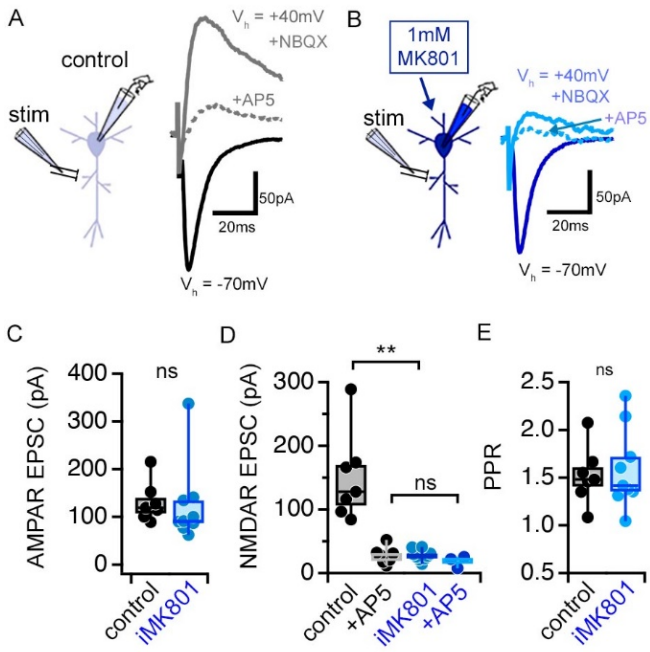

Supplementary Figure S1. MK801 (1mM) in the patch pipette (iMK801) completely blocks postsynaptic NMDARs. (**A-B**) Representative traces of EPSC recorded at a holding potential (V_h) of -70mV using control (*A*) or MK801-containing (*B*) pipette solution to measure AMPAR-mediated currents. EPSCs were recorded at a V_h of +40mV and in the presence of NBQX (10 μM) to measure isolated NMDAR-mediated currents. AP5 (20 μM) was subsequently added to the bath to confirm the NMDAR-dependence of EPSCs. EPSCs were sampled following a pre-experiment stimulation period that consisted of at least 45 pairs of pulses delivered at 0.1Hz at a V_h of -70mV. (**C**) AMPA-mediated EPSCs are no different between control and iMK801experiments. (**D**) NMDAR-mediated EPSCs are completely abolished by the presence of iMK801. (**E**) Paired pulse ratios (PPRs) measured at V_h -70mV are not altered by iMK801. Control n = 7 cells, 7 slices, 2 mice; Control +AP5 n = 7 cells, 7 slices, 2 mice; iMK801 n = 9 cells, 9 slices, 3 mice; iMK801 +AP5 n = 3 cells, 3 slices, 2 mice. ns $p > .05$, ** $p < .0001$ two-tailed t-test (*D, E*) or Mann-Whitney U test (*C*).

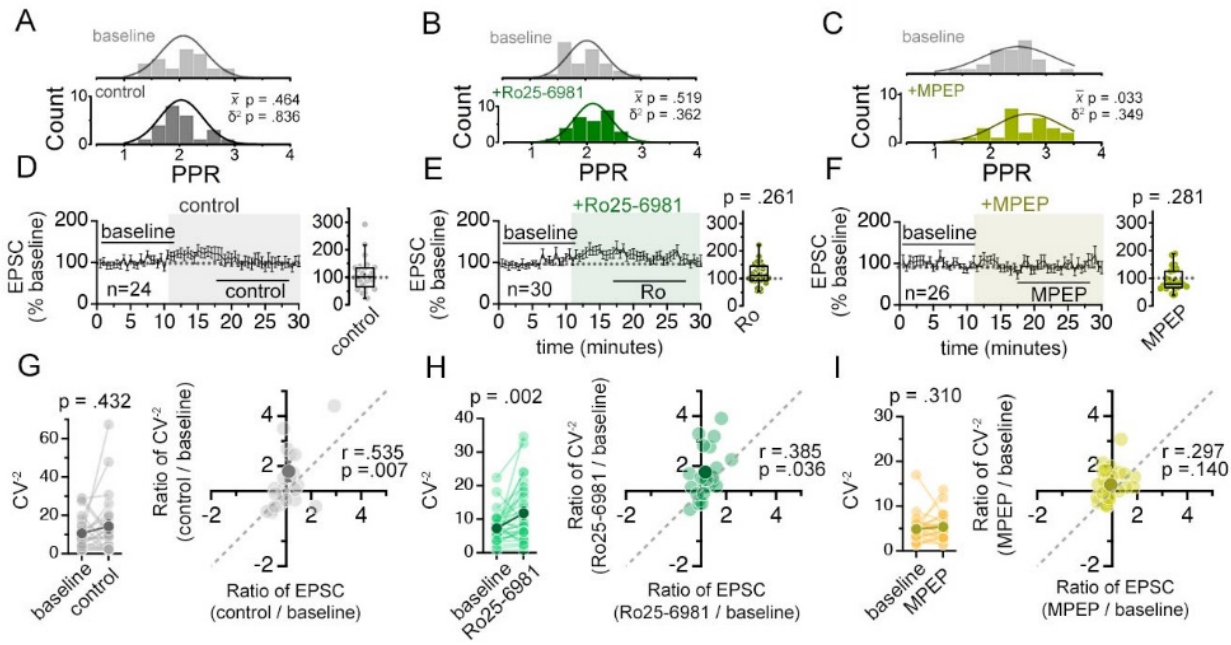

Supplementary Figure S2. Antagonists of GluN2B-containing NMDARs (Ro25-6981) or mGluR5 (MPEP) do not alter synaptic weight diversity. (**A-C**) Histograms of PPR distributions during the baseline (*top histogram*) and control aCSF or drug application (*bottom histogram*) were fit with single Gaussian curves. The p values obtained for the population mean ($\bar{x}$) (two tailed paired sample t-test for *A, B*, Wilcoxon signed rank test for *C*) and variance (δ^2) (one-tailed f-test for equal variances) comparing the baseline to the aCSF/drug application periods are shown in the graphs. (**D-F**) Plots of EPSC amplitudes (normalized to the baseline average) before and during the application of NMDAR antagonists (shaded area) where n is the number of inputs examined. Baseline and experimental periods are indicated (black bars). Box plots to the right show the summary of normalized EPSC amplitudes during the application of indicated inhibitors. P-values are the result of Mann-Whitney U tests comparing EPSC change drug application period to the corresponding period in control experiments. (**G-I**) Left: Mean (dark circles) and individual (light circles) CV^{-2} of EPSCs during the baseline and aCSF/drug application periods. P-values shown are the result of Wilcoxon signed rank tests. Right: Scatterplot of the relative change in CV^{-2} ($CV^{-2}_{experimental}/CV^{-2}_{baseline}$) against the relative change in EPSC amplitude ($EPSC_{experimental}/EPSC_{baseline}$) for the mean (dark circles) and individual inputs (light grey circles). Pearson's correlation coefficients (r) and p values are shown in the graph. Control n = 12 inputs, 24 cells, 11 mice; Ro25-6981 n = 30 inputs, 17 cells, 11 mice; MPEP n = 26 inputs, 13 cells, 5 mice.

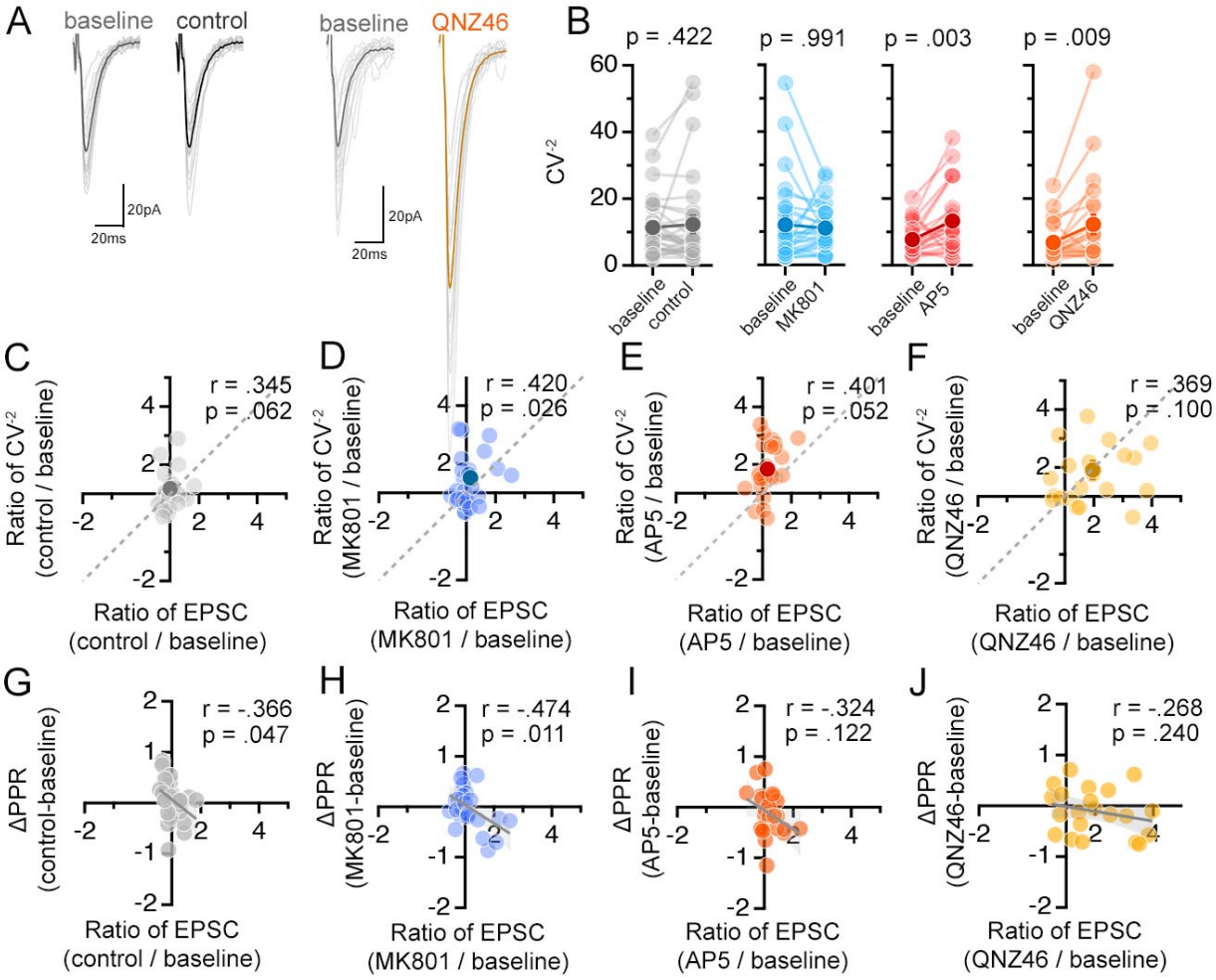

Supplementary Figure S3. NMDAR antagonists differentially influence presynaptic function. (**A**) Averaged (dark colors) and individual (light grey) EPSC traces during the baseline and experimental periods from a representative experiment. (**B**) Mean (dark circles) and individual (light grey circles) CV^{-2} of EPSCs during the baseline and aCSF/drug application periods. P-values are the result of Wilcoxon signed rank tests. (**C-F**) Scatterplot of the relative change in CV^{-2} ($CV^{-2}_{experimental}/CV^{-2}_{baseline}$) against the relative change in EPSC amplitude ($EPSC_{experimental}/EPSC_{baseline}$) for the mean (dark circles) and individual inputs (light circles). Pearson's correlation coefficients (r), p values, and the unity line (dashed) are shown in scatter plots. (**G-J**) Scatterplot of the difference in PPR ($PPR_{experimental}$-$PPR_{baseline}$) against the relative change in EPSC amplitude ($EPSC_{experimental}/EPSC_{baseline}$) for the mean (dark symbol) and individual inputs (light symbols). Linear fits (grey lines), Pearson's correlation coefficients (r), and p values are shown in scatter plots. Control = 30 inputs, 15 cells, 13 mice; MK801 = 28 inputs, 14 cells, 9 mice; AP5 = 24 inputs, 12 cells, 11 mice; QNZ46 = 22 inputs, 11 cells, 7 mice; Ro25-6981 n = 30 inputs, 17 cells, 11 mice; MPEP n = 26 inputs, 13 cells, 5 mice.

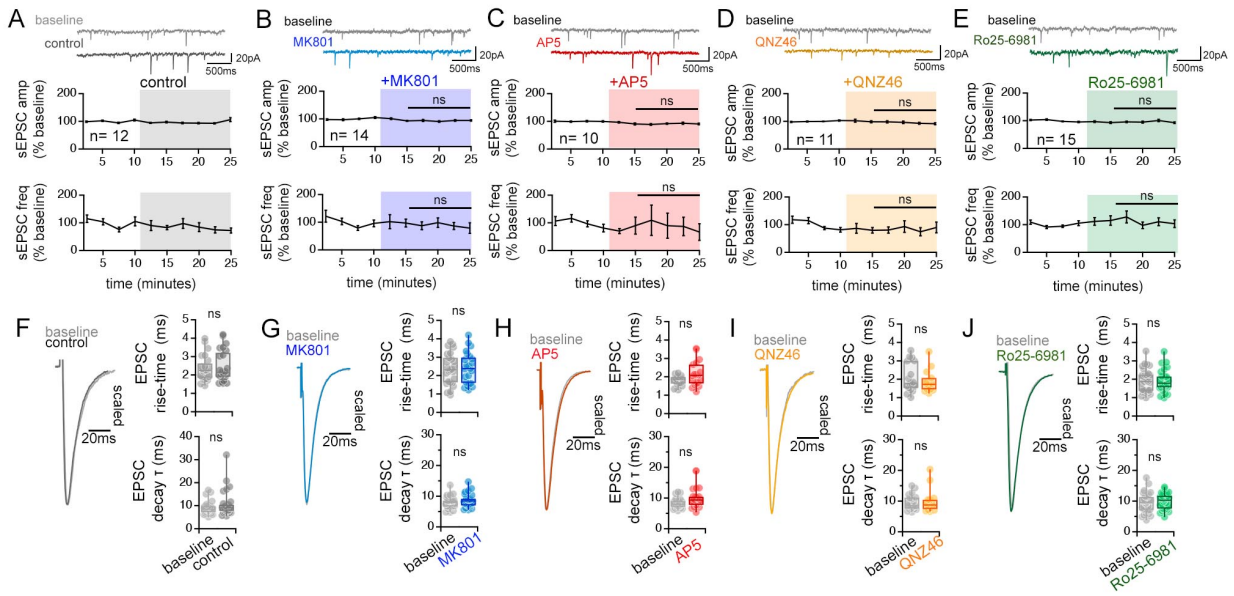

Supplementary Figure S4. NMDAR antagonists have little effect on spontaneous neurotransmission and the waveform of evoked EPSCs. (**A-E**) Representative traces and quantification of spontaneous EPSC amplitude and frequency recorded during the baseline and after applying control aCSF (*A*), MK801 (*B*), AP5 (*C*), QNZ46 (*D*), and Ro-256981 (*E*). Control n=12 cells, 10 mice; MK801 n = 14 cells, 9 mice; AP5 n = 10 cells, 9 mice; QNZ46 n = 11 cells, 8 mice; Ro25-6981 n = 15 cells, 10 mice. ns p > .05 one way ANOVA (amplitude), and Kruskal-Wallis ANOVA (frequency) comparing the normalized change during experimental periods across treatment conditions. (**F-J**) Left: Grand average waveforms of EPSCs recorded. Right: Box plots of EPSC risetime (top) and EPSC decay time constant (single exponential fit)(bottom) for baseline and control aCSF or drug application. ns p > .05 two tailed t-test or Mann-Whitney U tests. Control n = 24 inputs, 12 cells, 10 mice; MK801 n = 16 inputs, 11 cells, 11 mice; AP5 n = 26 inputs, 13 cells, 9 mice; QNZ46 n = 18 inputs, 9 cells, 6 mice; Ro25-6981 n = 32 inputs, 16 cells, 11 mice.

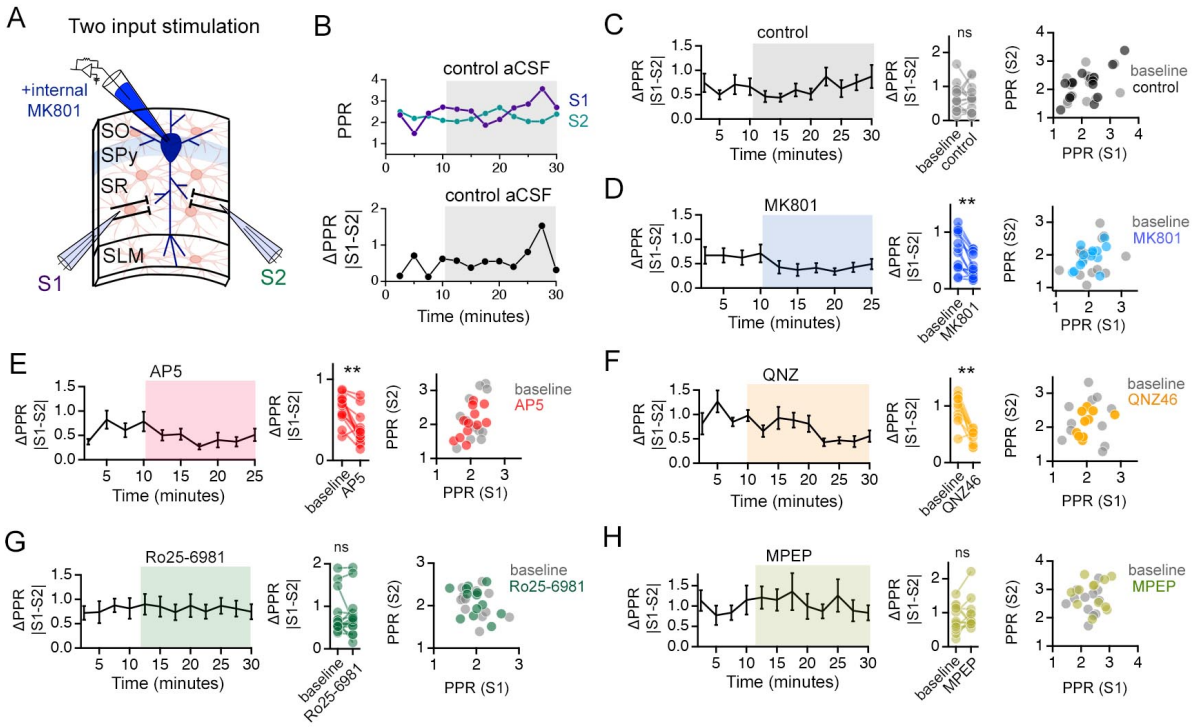

Supplementary Figure S5. NMDAR antagonists that target GluN2C-containing NMDARs reduce PPR disparity in the *stratum radiatum* (SR). (**A**) Illustration of the two-input stimulation configuration. Two independent inputs in the SR were sampled with interleaved stimulation. (**B**) The absolute difference between the PPRs of the two inputs sampled during a 2.5 min window (average of 5 sweeps) is referred to as ΔPPR ($|PPR_{S1}-PPR_{S2}|$) and is taken as a measure of variability of presynaptic strength. (**C-H**) Left: Time course of ΔPPR before and after application of antagonists. Middle: Summary plots of individual experiments comparing ΔPPR in baseline and during antagonist treatment. Right: Scatter plots comparing PPR of the two independent inputs normalized to the first EPSC amplitude for baseline and in the presence of the antagonists. ΔPPR is reduced by MK801 (*D*), AP5 (*E*), QNZ46 (*F*), but not by Ro25-6981 (*G*) or MPEP (*H*). Similarly, the scatterplots demonstrate distribution of average PPR values across pairs of inputs (S1 and S2) of PPRs by MK801, AP5 and QNZ46, all of which target GluN2C-containing NMDARs, but not by Ro25-6981 or MPEP that target GluN2B-NMDAR or mGluR5, respectively. ns $p > .05$, ** $p < .01$ Wilcoxon signed ranks test comparing baseline to drug application period. Control n = 15 pairs of inputs, 15 cells, 13 mice; MK801 n = 14 pairs of inputs, 14 cells, 9 mice; AP5 n = 12 pairs of inputs, 12 cells, 11 mice; QNZ46 n = 11 pairs of inputs, 11 cells, 7 mice; Ro25-6981 n = 15 pairs of inputs, 15 cells, 11 mice; MPEP n = 13 pairs of inputs, 13 cells, 5 mice.

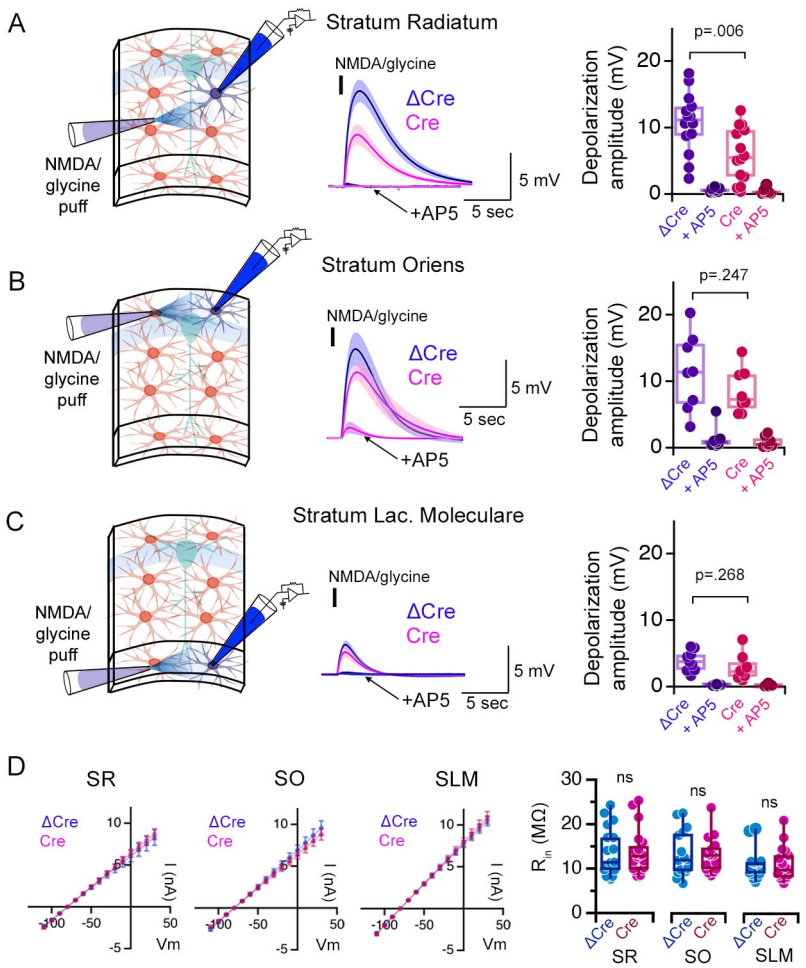

Supplementary Figure S6. Puff application of NMDA and glycine triggers the depolarization of astrocytes in hippocampal CA1 in acute slices. (**A**) Left: experimental setup. Middle: Local puff application (100 ms, black bar) of NMDA and glycine (1mM each) to astrocytes that are whole-cell patch clamped in the *stratum radiatum* (SR) elicits slow membrane depolarization (ΔCre, blue), which is prevented in the presence of AP5 (arrow). Once the depolarization is triggered, not only NMDARs but also other voltage-gated channels such as L-type calcium channels contribute to the slow depolarization (Letellier et al., 2016). The depolarization is substantially reduced when the same experiment is carried from Cre-expressing astrocytes as monitored by mCherry expression in slices infected with the AAV-GFAP104-nls-mCherry-Cre virus to knock-down astrocyte NMDARs in GRIN1 floxed mice (Cre, red). Right: Summary plot of the peak membrane depolarization in control virus infected (ΔCre) or NMDAR knock-down (Cre) slices in control aCSF or the presence of AP5. (**B-C**) Same as (*A*) except NMDA and glycine puff was applied to astrocytes patch-clamped in the *stratum oriens* (SO)(*B*) and *stratum lacunosum moleculare* (SLM)(*C*). NMDA/glycine puff-mediated depolarizations elicited in SO and SLM astrocytes are not sensitive to astrocyte NMDAR knockout. SR ΔCre n = 14 cells, 3 mice; SR Cre n = 14 cells, 3 mice. SO ΔCre n = 8 cells, 3 mice; SO Cre n = 8 cells, 3 mice. SLM ΔCre n = 9 cells, 2 mice; SLM Cre n = 8 cells, 2 mice. (**D**) Cre expression does not alter the input resistance (R_{in}) of astrocytes in any layer. IV relationships of ΔCre and Cre positive astrocytes in the SR, SO, and SLM to square voltage steps (left; 500ms duration) and quantification of R_{in} (right). SR ΔCre n = 17 cells, 8 mice; SR Cre n = 20 cells, 10 mice. SO ΔCre n = 16 cells, 10 mice; SO Cre n = 16 cells, 11 mice. SLM ΔCre n = 19 cells, 8 mice; SLM Cre n = 18 cells, 9 mice. ns $p > .05$, P values shown are the result of two-tailed t-tests or Mann-Whitney U tests.

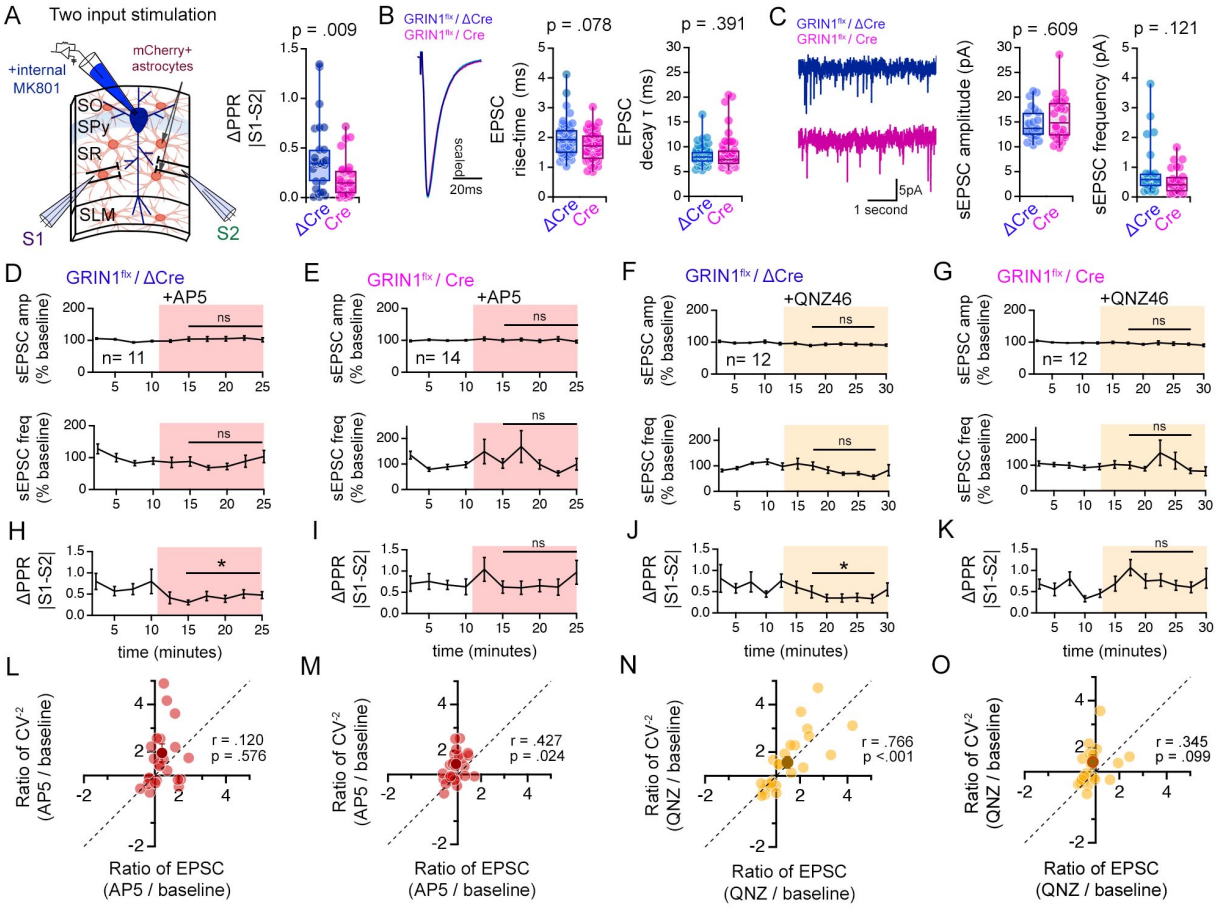

Supplementary Figure S7. Knock-down of GluN1 in hippocampal astrocytes selectively alters the PPR disparity without affecting the basic properties of synaptic transmission. (**A**) Left: Illustration of the experimental configuration of two-pathway stimulation approach to estimate PPR disparity in slices from GRIN1*flx/flx* mice infected with ΔCre or Cre virus. Right: Comparison of ΔPPR ($|PPR_{S1}-PPR_{S2}|$) between control ΔCre or Cre slices. PPR disparity (ΔPPR) is reduced in Cre infected slices compared to controls. p = .009, Mann-Whitney U test. ΔCre n = 29 pairs of inputs, 29 cells, 8 mice. Cre n = 28 pairs of inputs, 28 cells, 6 mice. (**B**) Left: Grand average waveforms of EPSCs recorded. Right: Box plots of EPSC risetime and EPSC decay time constant (single exponential fit). Each data point represents the average waveform of at least 5 sweeps of EPSCs. ΔCre n = 46 inputs, 23 cells, 8 mice. Cre n = 41 inputs, 21 cells, 6 mice. (**C**) Left: Representative traces of spontaneous EPSC (sEPSC) recordings from control ΔCre (blue) or Cre (red) slices. Right: Boxplots of sEPSC amplitude and frequency measured in ΔCre or Cre-infected slices. P values shown are the result of Mann-Whitney U test. ΔCre n = 23 cells, 5 mice. Cre n = 26 cells, 5 mice. (**D-G**) Normalized sEPSC amplitude (top) and frequency (bottom) during baseline and in the presence of AP5 or QNZ46 in control ΔCre or Cre-infected slices. Neither sEPSC amplitude nor frequency is not affected by AP5 or QNZ46. Two tailed t-test or Mann-Whitney U test, comparisons made between ΔCre vs. Cre normalized values in post drug period indicated. (**H-K**) ΔPPR ($|PPR_{S1}-PPR_{S2}|$) measurements during baseline and in the presence of AP5 or QNZ46 in control ΔCre or Cre-infected slices. The decrease in PPR disparity triggered by AP5 (*H*) and QNZ46 (*J*) is prevented upon knock-down of astrocyte NMDARs. * $p < .05$ Wilcoxon signed ranks test. ΔCre + AP5 n = 12 pairs of inputs, 12 cells, 6 mice. Cre + AP5 n = 14 pairs of inputs, 14 cells, 5 mice. ΔCre + QNZ46 n = 12 pairs of inputs, 12 cells, 5 mice. Cre + QNZ46 n = 12 pairs of inputs, 12 cells, 6 mice. (**L-O**) Scatterplot of the relative change of CV^{-2} ($CV^{-2}_{experimental}/CV^{-2}_{baseline}$) against the relative change in

EPSC amplitude ($EPSC_{experimental}/EPSC_{baseline}$) for the mean (dark symbol) and individual inputs (light symbols). Dashed lines show positive unity line. Pearson's correlation coefficients (r) and p values are shown in scatter plots. N values are the same as *H-K*.

(*Supplementary Figure S7 legend continued from previous page*)

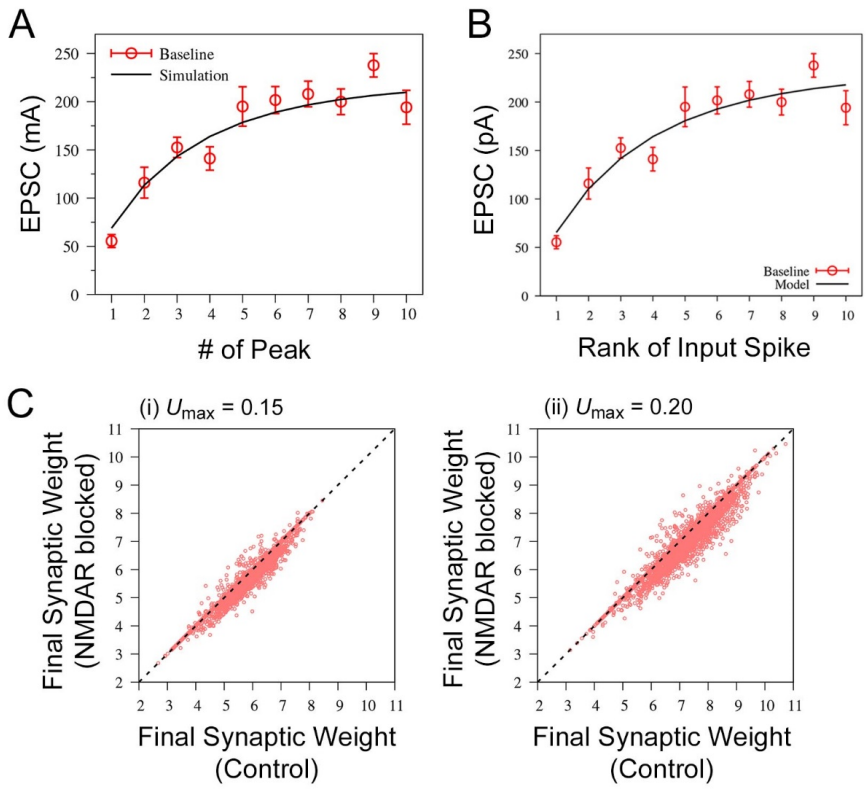

Supplementary Figure S8. Additional data for mathematical modelling experiments exploring the impact of presynaptic release probability variance on synaptic plasticity. (**A,B**) The best-fits to the experimentally obtained peak EPSC amplitudes of responses triggered by a 20Hz spike train in the BCM-like model (A) and the spiking neuron model (B). The best-fit parameters are τ_f = 540 ms, τ_{rec} = 20 ms, U_{max} = 0.1 and $w(0)$ = 332 in (A), and τ_f = 980 ms, τ_{rec} = 25 ms, U_{max} = 0.1 and $w(0)$ = 6.7 in (B). (**C**) A comparison of the synaptic weight changes observed in response to Poisson spike trains in control condition versus the NMDAR-blocked condition (reduced presynaptic release probability variance) for simulations at (i) $U_{\max}$ = 0.15 and (ii) $U_{\max}$ = 0.20. Final synaptic weight above the initial synaptic weight value of $w(0)$ = 6.7, is considered potentiation and below $w(0)$ = 6.7 is considered depression.

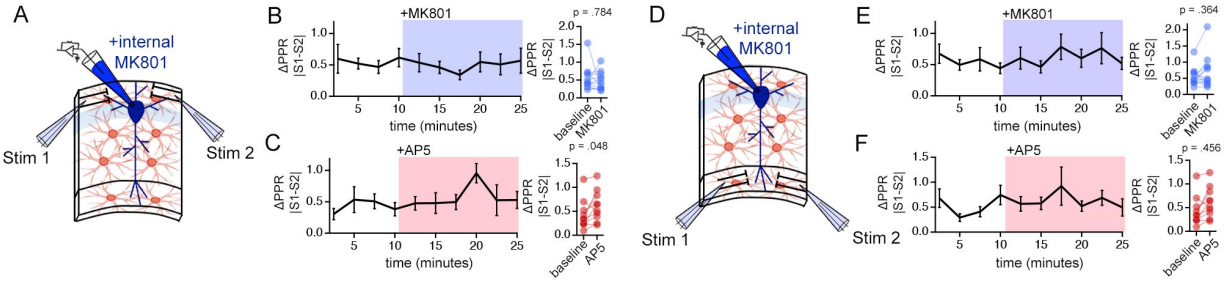

Supplementary Figure S9. MK801 and AP5 do not alter PPR disparity in the *stratum oriens* (SO) or the *stratum lacunosum moleculare* (SLM). (**A**) Illustration of the two-input stimulation configuration in SO. (**B,C**) Left: PPR disparity [ΔPPR ($|PPR_{S1}-PPR_{S2}|$)] during baseline and in the presence of MK801 (*B*) or AP5 (*C*). Right: Summary plot of ΔPPR. Neither MK801 nor AP5 application influences the PPR disparity. (**D-F**) Same experiments as described for (*A-C*) carried out in SLM. Similarly to SO recordings, MK801 and AP5 have no effects of PPR disparity in SLM. P-values are the result of Wilcoxon signed rank tests. SO MK801 n = 12 pairs of inputs, 12 cells, 6 mice; SO AP5 n = 10 pairs of inputs, 10 cells, 7 mice; SLM MK801 n = 13 pairs of inputs, 13 cells, 8 mice; SLM AP5 n = 12 pairs of inputs, 12 cells, 6 mice.